

Three-dimensional density field of a screeching under-expanded jet in helical mode using multi-view digital holographic interferometry

Olivier Léon, David Donjat, François Olchewsky, Jean-Michel Desse, François Nicolas, Frédéric Champagnat

▶ **To cite this version:**

Olivier Léon, David Donjat, François Olchewsky, Jean-Michel Desse, François Nicolas, et al.. Three-dimensional density field of a screeching under-expanded jet in helical mode using multi-view digital holographic interferometry. Journal of Fluid Mechanics, 2022, 947, pp.A36. 10.1017/jfm.2022.659 . hal-03822531

HAL Id: hal-03822531
https://hal.science/hal-03822531

Submitted on 20 Oct 2022

HAL is a multi-disciplinary open access archive for the deposit and dissemination of scientific research documents, whether they are published or not. The documents may come from teaching and research institutions in France or abroad, or from public or private research centers.

L'archive ouverte pluridisciplinaire **HAL**, est destinée au dépôt et à la diffusion de documents scientifiques de niveau recherche, publiés ou non, émanant des établissements d'enseignement et de recherche français ou étrangers, des laboratoires publics ou privés.

3D density field of a screeching under-expanded jet in helical mode using multi-view Digital Holographic Interferometry

O. Léon[1] †, D. Donjat[1], F. Olchewsky[2], J.-M. Desse[2], F. Nicolas[3], F. Champagnat[4]

[1]ONERA/DMPE, Université de Toulouse, 2 avenue Edouard Belin, Toulouse, France

[2]ONERA/DAAA, Laboratoire de Mécanique des Fluides de Lille - Kampé de Fériet, 59000 Lille, France

[3]ONERA/DAAA, Université Paris Saclay, 92190 Meudon, France

[4]ONERA/DTIS, Université Paris Saclay, 91123 Palaiseau, France

A synchronized multi-axis Digital Holographic Interferometry setup is presented for the study of 3D flow fields with large density gradients. This optical configuration provides instantaneous interferograms with fine spatial resolution in 6 directions of projection. A regularized tomographic approach taking into account the presence of possible shock waves is furthermore considered to reconstruct 3D density fields. Applied to a screeching under-expanded supersonic jet with helical dynamics, this setup is used to provide dense optical phase measurements in the initial region of the jet. The jet mean density field is shown to be satisfactorily estimated with sharply resolved density gradients. In addition, an approach based on azimuthal Fourier transform and snapshot Proper Orthogonal Decomposition (POD) applied to the instantaneous flow observations is proposed to study the main coherent dynamics of the jet. Relying on a cluster analysis of the azimuthal POD mode coefficients, a reduced dynamical model in the POD mode phase space is used as an approximation of the two observed limit cycles. A clear 3D representation of the density field of a helical instability associated with screech mode C is then evidenced, with two equally-probable directions of rotation. Switching between the two directions is reported, highlighting intermittency in the feedback loop. This helical structure is particularly seen to extend to the jet core, driving its internal dynamics and inducing out-of-phase density fluctuations between the outer and inner shear layers. These out-of-phase motions are related to the non-uniform radial distribution of fluctuation phase associated with the outer-layer Kelvin–Helmholtz instability wave.

1. Introduction

Supersonic jets are complex flows exhibiting a variety of interactions between strong shock waves, small and large scale turbulent structures, internal modes and externally-propagating acoustic waves. A particular example is found in under-expanded supersonic jets where such complex interactions can generate an aero-acoustic feedback mechanism known as screech (Powell 1953), locking the jet dynamics into different possible modes or limit cycles. The complexity of the mechanisms involved has prevented the development of accurate prediction tools and experimental studies are still needed to better understand the main 3D dynamics of these jets.

However, this complex environment poses metrological challenges. One promising way to address the problem is to consider seedless optical techniques for probing the jet density field. Among the different approaches that have been proposed in the literature, one of the optically

† Email address for correspondence: olivier.leon@onera.fr

simplest technique is tomographic Background Oriented Schlieren (BOS) (Atcheson et al. 2008; Nicolas et al. 2016), which has been successfully applied to the study of supersonic jets by Nicolas et al. (2017) using a multi-camera setup. Tomographic BOS can nevertheless be limited in terms of spatial resolution since the cameras are focused on the background and not on the flow of interest, but also because of spatial filtering induced by image correlation algorithms. Another optical technique used by Panda & Seasholtz (1999) to provide density measurements in under-expanded jets is Rayleigh scattering. This technique offers fine spatial measurement resolution with significant accuracy. However, the measurement is pointwise, which is not ideal for the analysis of 3D coherent structures, and the results can be particularly sensitive to Mie scattering.

The present work investigates the use of synchronized multi-axis Digital Holographic Interferometry (DHI) for the study of the average and dynamical state of an under-expanded screeching supersonic jet in helical mode. This approach provides multiple dense observations of the flow at different angles as in tomographic BOS, but with a finer spatial resolution. It is then demonstrated how these flow projections can be leveraged to expose and analyze the main 3D coherent structures associated with the observed helical instability.

1.1. *Multi-view Digital Holographic Interferometry*

Applied to transparent media, Holographic Interferometry (HI) provides a means of evaluating the phase variations of an optical wavefront passing through a field of non-homogeneous refractive index in comparison with a reference state (Schnars et al. 2014; Picart et al. 2015). HI is then a line-of-sight technique that provides integral projections of a flow field and satisfactory estimation of an instantaneous 3D density field thus requires simultaneous multi-directional acquisitions.

In the context of non-homogeneous 3D flows, this idea was first followed some fifty years ago, with early works described by Matulka & Collins (1971) and Sweeney & Vest (1974). These authors demonstrated that several interferograms obtained from different viewing angles using holographic plates could be successfully processed to estimate asymmetric density fields by solving a set of equations involving fringe number functions. At the time, recording devices were mainly analog and the evaluation of the fringe number functions yielded by the interfering holograms could only be performed visually, ultimately providing measurements with a reduced spatial resolution.

The rise of digital recording devices has naturally led to significant improvements in this technique. Early applications to flow visualization were reported by Watt & Vest (1987) who used a digital camera to record the interferometric pattern obtained by illuminating a double-exposed holographic plate. Post-processing of the fringe pattern could then be performed numerically, thus providing accurate and well-resolved instantaneous maps of interferometric phase-delays. Relying on this approach, Snyder & Hesselink (1988) and Watt & Vest (1990) later performed tomographic reconstructions of instantaneous density fields induced by a helium jet using several viewing angles. Snyder & Hesselink (1988) used 18 instantaneous interferograms distributed around the jet axis while Watt & Vest (1990) relied on two orthogonal holographic plates from which multi-angular views of the holographic interferograms could be retrieved a posteriori with different camera orientations. At the time, this approach was already termed digital HI for the interferograms were digitized. It is noted however that, nowadays, DHI rather refers to the direct acquisition of digital holograms by a camera, with no need for a holographic plate (Schnars et al. 2014). Consequently, in this work, DHI will refer only to this recent definition, while the older approach will be referred to as "digitized HI".

Tomographic digitized HI was further considered by Timmerman & Watt (1995) and Timmerman et al. (1999) to study supersonic jets, relying on the initial single-view optical

setup proposed by Lanen et al. (1992). A digitized tomographic holographic interferometer was designed to simultaneously record on a single holographic plate 6 to 9 different holograms of the flow of interest using a pulsed laser. A phase-stepping approach was used to unambiguously determine phase maps associated with the digitized interferograms and tomographic reconstruction was performed relying on an algebraic reconstruction method.

Interestingly, at about the same time, another tomographic interferometric technique was considered by Söller et al. (1994) and Dillmann et al. (1998) to study supersonic jets. These authors relied on a single-view Mach–Zehnder interferometer set to an infinite fringe mode (Smits 2012) to estimate phase variations from the interferograms. No holographic plate was required since the interferograms could be directly imaged on the camera sensor. Only one viewing angle was considered with this setup and tomographic reconstructions were performed on mean flows, assuming flow axisymmetry.

This digital interferometric approach shares strong similarities with the holographic interferometric technique previously discussed since they both yield an interferometric pattern containing information about phase variations across the flow field. Yet, the holographic approach can be considered less stringent on the constraints applying to the optical path of the reference beam (Smits 2012). Indeed, the double exposure technique in the holographic method ensures that the phase variations observed are exactly the ones induced by the flow itself, whereas in the case of interferometry the optical path of the reference beam is of prime importance. Nevertheless, this technical difference vanishes if one considers a Mach–Zehnder interferometer used in a finite fringe mode and if fringe patterns are made to interfere with a reference state acquired without flow. This exactly corresponds to DHI, where holograms are acquired by cameras (Schnars et al. 2014). This approach was recently followed and detailed by Sugawara et al. (2020) who also studied the mean structure of supersonic under-expanded jets. In the latter work, a single view was considered and tomographic reconstructions were again obtained assuming axisymmetry, relying on the inverse Abel transform. Single-view DHI with Abel transform has also been recently applied by Rodrigues et al. (2021) to study under-expanded supersonic jets, but using high-speed cameras in an attempt to resolve temporal fluctuations in optical phase. Finally, Doleček et al. (2013) and Doleček et al. (2016) studied heated synthetic jets using a single-axis DHI setup and relied on a phase-averaging technique to acquire holograms of the periodic flow at different viewing angles. Tomographic reconstructions were then obtained by these authors relying on a classical inverse Radon transform.

This fully digital approach to holographic interferometry is nowadays possible due to the increased resolution of imaging sensors and the reduction in pixel size. The holograms are then directly acquired by high-definition camera sensors and the final interference phase maps can be retrieved by simple spectral post-processing. These technical refinements therefore now offer the opportunity to revisit multi-view holographic interferometry, in a way that shares similarities with the recently developed tomographic BOS technique, and to benefit from significant improvements made in tomographic reconstruction. Based on this idea, the first objective of this work is to detail in sections 2 and 3 the development of a multi-axis DHI configuration adapted to the study of unsteady complex 3D jet flows with large density gradients in a limited field of view.

1.2. *Under-expanded screeching supersonic jets*

The flow considered in this work is a round supersonic under-expanded jet issuing from a choked nozzle. Such a jet is obtained when a gas is exhausted through a contoured converging nozzle in an non-ideally expanded manner, i.e. when the flow static pressure at the exit, p_0, is higher than the ambient one, p_a. The operating condition can then be defined by the Nozzle Pressure Ratio NPR = p_{t0}/p_a where p_{t0} is the stagnation (or total) pressure at the nozzle

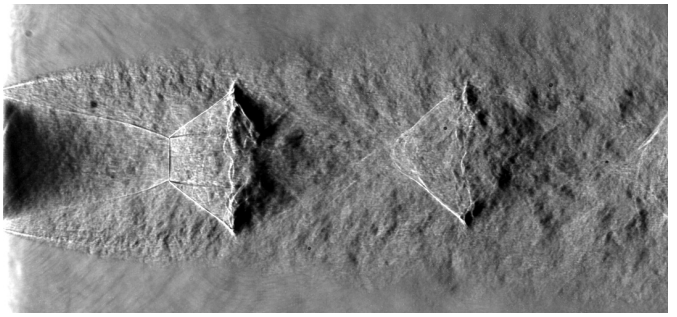


Figure 1: Spark schlieren visualization of an under-expanded supersonic jet at NPR = 5 and a total temperature of 293 K.

exit. Equivalently, the ideally expanded Mach number M_j can be used and is defined as

$$M_j = \left(\frac{2}{\gamma - 1} \left[\mathrm{NPR}^{\frac{(\gamma-1)}{\gamma}} - 1 \right] \right)^{\frac{1}{2}} \tag{1.1}$$

where γ is the heat capacity ratio taken equal to 1.4 for dry air.

A detailed description of the average structure of under-expanded jets can be found in the review provided by Franquet et al. (2015). As illustrated by the schlieren visualization shown in figure 1 for a jet at NPR = 5, under-expanded jets feature quasi-periodic shock-cell structures generated by successive expansion and compression waves trapped in the jet plume. For such a value of NPR, the Mach disk induced by a Mach reflection on the centerline is particularly visible in the first cell. The average structure of this type of jet has been extensively studied in the literature using such schlieren photographs, giving easy access to geometric parameters such as the average spacing of the shock cells and the diameter of the Mach disk.

One particular aspect of under-expanded jets is the possible generation of an aeroacoustic feedback loop, inducing an extremely tonal screech noise (Raman 1999; Edgington-Mitchell 2019). The basic understanding of this phenomenon is that the natural instability waves of the jet outer shear layer interact with the shock-cells to produce upstream-traveling free-stream acoustic or internally-guided waves that excite the jet shear layer at the nozzle lip (Gojon et al. 2018; Edgington-Mitchell et al. 2018; Nogueira et al. 2022), which is a high-receptivity region of the jet. This resonant closed-loop mechanism then amplifies the most unstable waves, providing a highly frequency-selective mechanism that may be understood as a global instability (Edgington-Mitchell et al. 2021; Nogueira et al. 2021). Interestingly, different frequencies are selected when varying the NPR and sharp frequency jumps are usually observed, permitting the identification of different screech modes. Following the terminology proposed by Powell (1953), the four main modes are labeled A, B, C and D. Each mode was reported by Powell et al. (1992) to present different azimuthal structures, that were deduced to be mainly axisymmetric, flapping, helicoidal and flapping with rotation respectively. A variety of measurement techniques have been used to study these modes, with schlieren visualizations and acoustic measurements being the most common ones (see for example André et al. (2011)). Density fields, however, are more rarely studied: among the few references, Panda & Seasholtz (1999) relied on Rayleigh scattering to obtain pointwise measurements while Nicolas et al. (2017) and Lanzillotta et al. (2019) used tomographic BOS to evidence the average spatial structure of two screech modes.

Overall, field measurements providing detailed quantitative descriptions of under-expanded screeching jets are relatively scarce in the literature, particularly when it comes

to the structure of the jet over the first few nozzle diameters and the flow dynamics in the vicinity of the Mach disk. Notable work on this point was performed by Edgington-Mitchell et al. (2014a) who conducted a planar PIV experiment to describe the velocity field of an under-expanded jet in helical screech mode C, at NPR = 4.2, with a particular emphasis on the embedded annular shear layer present behind the first Mach disk. This work highlighted the influence of azimuthal large-scale structures developing in the external jet shear layer on the reflected shock, which was then hypothesized to force the internal annular jet shear layer in a coherent but out-of-phase manner. This dynamical link between the structures found in the outer and inner jet shear layers, and more generally between the main screech instability and inner jet motions, has not been experimentally reexamined to the knowledge of the present authors. Using the capability of the developed multi-view DHI setup to access the azimuthal content of a density field, the second objective of the present work pursued in section 4 is to provide another quantitative look at the dynamical features occurring in screeching under-expanded jets in helical mode.

2. Digital Holographic Interferometry and 3D density field estimation

DHI being a line-of-sight technique, it naturally requires an appropriate inversion methodology to reconstruct 3D density fields. Furthermore, the raw measurements provided by DHI are interferometric patterns that need to be converted to relative optical thicknesses or phase variations before tomographic processing. This section thus discusses the different physical notions required to understand the methodology followed to develop the present multi-view DHI setup.

2.1. *Digital Holographic Interferometry for transparent media*

Considering a 3D flow field of refractive index $n_\lambda(\boldsymbol{x})$ at a wavelength λ, a coherent wavefront passing through will be distorted, inducing variations in optical path lengths (OPL, noted Λ) compared to a reference situation without flow. The OPL of a monochromatic light ray following a path C is defined as

$$\Lambda = \int_C n_\lambda(s)\,\mathrm{d}s\ , \tag{2.1}$$

where s is a curvilinear abscissa. The field of refractive index being related to the flow density field $\rho(\boldsymbol{x})$ by the Gladstone–Dale relation, this equation can be written as

$$\Lambda = \int_C (\mathcal{K}_\lambda \rho(s) + 1)\,\mathrm{d}s \tag{2.2}$$

where $\mathcal{K}_\lambda$ refers to the Gladstone–Dale constant of the fluid at the considered wavelength λ. The variation of OPL $\delta\Lambda$ with respect to a reference flow situation with uniform density ρ_0 then writes

$$\delta\Lambda = \mathcal{K}_\lambda \int_C (\rho(s) - \rho_0)\,\mathrm{d}s\ . \tag{2.3}$$

The OPL variations may be related to phase variations $\delta\phi$ in the initial wavefront using the dispersion relation, yielding

$$\delta\phi = 2\pi \frac{\delta\Lambda}{\lambda}\ . \tag{2.4}$$

DHI provides a way to measure these integrated phase variations $\delta\phi$ by evaluating the phase difference of two digital holograms obtained for the two different flow states. This

phase difference is equivalent to the interference phase obtained using an analog holographic approach where these holograms are made to interfere by re-illumination. Details about the formation of holograms and their processing may be found in references such as Schnars et al. (2014) or Picart et al. (2015), and only the basics are reminded here. A hologram is the result of the interference of two light waves in an observation plane: a reference wave traversing a transparent medium that does not change over time and a second wave that passes through the unsteady transparent medium of interest. It can be noted that holographic techniques are most commonly used with opaque or translucent objects, but the physical principles remain the same. Assuming the use of a monochromatic light, the complex amplitude of the reference wavefront in the observation plane (η, ξ) can be expressed as

$$E_r(\eta, \xi) = a_r(\eta, \xi) \exp\left[\mathrm{i}\phi_r(\eta, \xi)\right] \tag{2.5}$$

where a_r refers to the real amplitude, ϕ_r to the phase of the reference wave and i is the imaginary unit. Similarly, the measurement wavefront reaching the observation plane after traversing the transparent media (the object) and thus integrating the associated phase changes is written as

$$E_o(\eta, \xi) = a_o(\eta, \xi) \exp\left[\mathrm{i}\phi_o(\eta, \xi)\right] \tag{2.6}$$

where a_o and ϕ_o refer to the real amplitude and the phase of the measurement wave. These two waves interfere in the observation plane and the resulting light intensity captured by the camera sensor is given by

$$I(\eta, \xi) = |E_r + E_o|^2 \tag{2.7}$$

$$= \underbrace{|E_r|^2 + |E_o|^2}_{0 \text{ order}} + \underbrace{E_r^* E_o}_{+1 \text{ order}} + \underbrace{E_r E_o^*}_{-1 \text{ order}} \tag{2.8}$$

where the superscipt $\cdot^*$ refers to the complex conjugate. Three diffraction order terms can be identified in this equation, terms that will be further discussed and illustrated in section 2.3. This expression can also be written as

$$I(\eta, \xi) = a_r^2 + a_o^2 + 2a_r a_o \cos(\phi_o - \phi_r), \tag{2.9}$$

showing that the digital hologram is made of a background (the 0 order term), determined by the intensity of the two wavefronts, and an interference term varying with the phase difference $\phi_o - \phi_r$. The interference pattern obtained depends on the direction of propagation of the two waves: in an "off-axis" DHI setup, i.e. when the two waves are made to propagate in slightly different directions, a spatial carrier wave is formed permitting efficient isolation of the phase difference term from the 0 order term as presented in section 2.3.

Post-processing the interferograms then allows the estimation of phase difference maps $\Delta\phi(\eta, \xi) = \phi_o - \phi_r$ in the observation plane for one flow state. As a consequence, the phase difference $\delta\phi$ between two flow states, required to evaluate the OPL variations $\delta\Lambda$ using (2.4), can be simply estimated by the difference

$$\delta\phi(\eta, \xi) = \Delta\phi_n - \Delta\phi_0 . \tag{2.10}$$

Here, $\Delta\phi_n$ refers to the holographic phase of the flow of interest acquired at an instant t_n and $\Delta\phi_0$ to a reference holographic phase, typically obtained without flow. As mentioned in the introduction, a clear advantage of this approach over traditional interferometric methods is that the estimated phase variation $\delta\phi$ does not depend on ϕ_r, the phase of the reference wave, since it is canceled in the subtraction process.

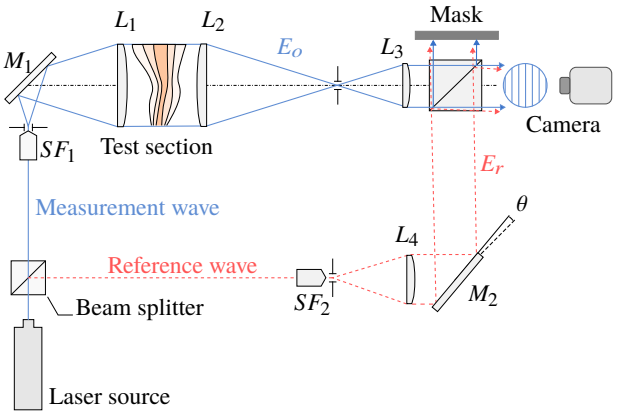


Figure 2: Schematic of a single-camera Mach–Zehnder interferometer used to perform off-axis Digital Holographic Interferometry. M_i refers to flat mirrors, L_i to spherical lenses and SF_i to spatial filters.

2.2. *Mach–Zehnder interferometric setup for DHI*

Different optical setups may be considered to perform off-axis DHI with transparent media. As emphasized by Desse & Olchewsky (2016), when studying flows with large density gradients one particularly needs to account for the sensitivity of the apparatus and possible shadow effects arising from light refraction. Indeed, the presence of shock waves in the flow was shown to cast shadows in the holograms, with a detrimental effect on phase estimation. This was particularly observed using a Michelson interferometer which relies on a double-pass of the measurement wave through the flow of interest. In contrast, with a Mach–Zehnder interferometer, the measurement wave only traverses the flow once. As a result, the sensitivity is halved, but shadow effects can be greatly reduced by properly focusing the imaging system on the flow. Based on this experimental result, a similar optical setup is considered in the present work.

A classical setup for off-axis DHI relying on a Mach–Zehnder interferometer is schematically illustrated in figure 2. The laser beam is split in two by a beam splitter cube. The reference beam is spatially filtered (SF_2), expanded and directed to a recombination cube (L_4, M_2). This reference wave traverses a quiescent atmosphere with uniform density and its path towards the recombination cube is controlled using a flat mirror (M_2). The angle θ of this mirror controls the direction of propagation of the reference wave relative to the measurement wave after recombination and its fine-tuning is necessary to generate a spatial carrier wave as discussed in section 2.1. The measurement wave is also filtered (SF_1) and expanded to traverse the measurement volume in parallel rays (M_1, L_1) before being reduced using an afocal optical setup (L_2, L_3) and reaching the recombination cube. Both waves then illuminate the camera sensor to create a digital hologram, with the fringe spacing and orientation of the spatial carrier being controlled by θ.

A practical implementation of this Mach–Zehnder interferometer for the analysis of a supersonic jet will be presented in section 3. At this stage, some important constraints associated with this optical setup can be emphasized. First, the size of the volume of interest is limited by the size of the spherical lenses L_1 and L_2, usually limiting the technique to flows a few centimeters wide. Second, the laser source needs to produce a light with sufficient coherence length to ensure proper formation of an interferometric pattern on the camera sensor during exposure time. For high-speed flows such as the one investigated in this work and for which short-time illumination is required to obtained instantaneous snapshot

holograms of the flow, specific pulsed lasers with long coherence length are then needed. Finally, vibrations in the optical system can be particularly detrimental to the measurement and care must be taken to reduce them as much as possible. For example, it is necessary to ensure a certain level of steadiness in the density field traversed by the reference wave as well as an absence of temporal drifts that may be induced by such vibrations.

2.3. *Interferograms processing*

Once the digital holograms are acquired, phase maps need to be estimated. Two steps are required with the present approach: phase evaluation and phase map unwrapping.

2.3.1. *Phase map evaluation*

Two main approaches are usually considered to recover the phase distribution $\Delta\phi$ from the interferometric image associated with equation (2.7): temporal phase-stepping (or phase-shifting) and spectral filtering (Picart et al. 2015). The latter method is considered in the present work since a reference state (without flow) can be easily acquired, permitting phase estimation with a single acquisition and enabling the analysis of instantaneous density distributions in high-speed flows with an optical setup of reduced complexity.

The main idea of this technique is to isolate the +1 diffraction order from equation (2.8) and to evaluate its phase. This is possible in off-axis DHI because of the use of a spatial carrier frequency yielding a clear separation of the different diffraction orders in Fourier space. For example, figure 3(a) displays an interferogram acquired in a reference state, i.e. without flow, with the apparatus later described in section 3. In this figure, the (x, z) coordinate system used is deduced from that of the observation plane (η, ξ) by application of the optical magnification factor of the apparatus, with an origin located at the center of the jet exit plane. An inset highlights the fringe pattern induced by the off-axis modulation and its chosen orientation which is approximately at 45°. The amplitude of the 2D Fourier transform of this image is represented in figure 3(b), using a logarithmic scale. The different diffraction orders are easily identified and can thus be individually filtered, as originally proposed by Takeda et al. (1982) in a different context.

Different spectral filter shapes and functions may be considered. In this work, the pupil of the optical setup was verified to produce an Airy pattern smaller than the pixel size of the camera, thus such that no selection limitation in the Fourier spectrum appears. A classical rectangular filter was then chosen since it provided consistent results for all the cases considered. After application of this filter and inverse Fourier transform, a filtered hologram I_F isolating the +1 diffraction order is obtained, writing

$$I_F(\eta, \xi) = \mathscr{F}^{-1}\left(W(k_\eta, k_\xi)\,\mathscr{F}(I)\right) \tag{2.11}$$

where $\mathscr{F}$ refers to Fourier transform and $W(k_\eta, k_\xi)$ is the filtering window in the wavenumber plane. An example of such a filtering is given in figure 3(b), where the red rectangle indicates the bounds of the chosen filter. The 0 order is concentrated at the origin and the selected window discards this region while retaining about a quarter of the 2D spectrum. This window was furthermore chosen to isolate the +1 diffraction order for the cases where the flow of interest was in the measurement beam. An example of interferometric pattern captured in this situation is shown in figure 3(c), highlighting the large changes in fringe orientation induced by the inhomogeneous density field. The associated 2D spectrum is displayed in figure 3(d), where the previous filtering window is also shown. Compared to the reference state, the variations in the fringe pattern induce a spread of the spectral support of the +1 order, but the selected window still captures most of the associated content.

The holographic phase $\Delta\phi$ is then deduced (modulo 2π) from the filtered hologram I_F by

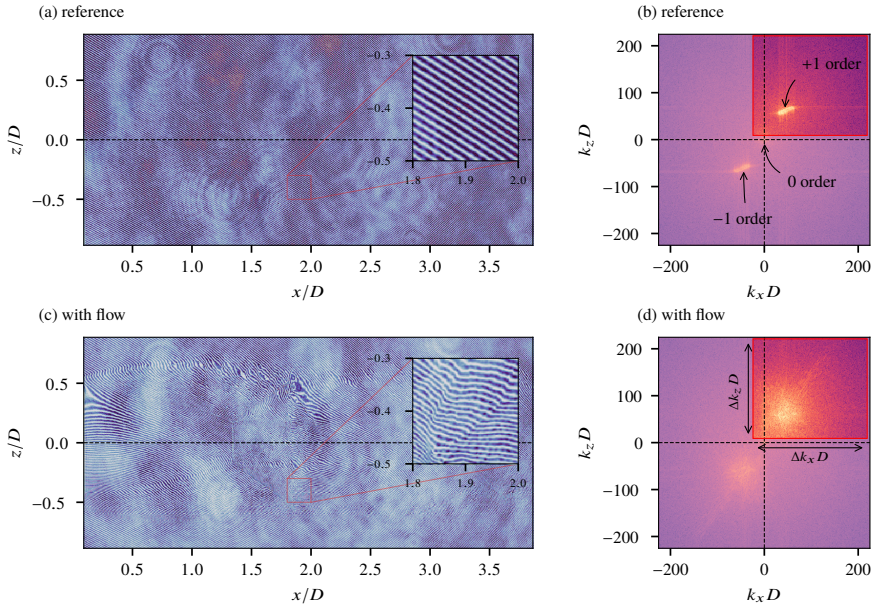


Figure 3: Examples of (a,c) digital holograms in the aerodynamic plane (x, z) and (b,d) associated 2D spectra obtained respectively without flow (reference state) and with an under-expanded supersonic jet (NPR = 5) in the measurement beam using the experimental setup described in section 3. In (a) and (c), the insets provide local magnifications on the fringe patterns. In (b) and (d), a logarithmic scale on the spectrum amplitude was used and the parts of the spectra that are filtered out are colored using lighter tones. k_i refers to a wavenumber in the ith direction and D is the diameter of the jet nozzle exit.

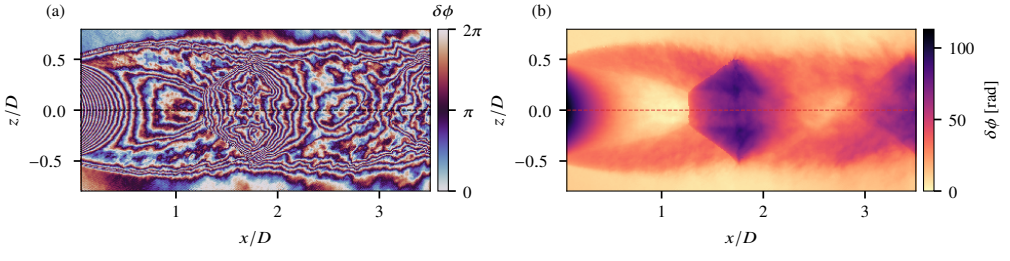


Figure 4: (a) Folded phase difference map deduced from the digital holograms shown in figure 3 and (b) the corresponding map of unwrapped phase difference obtained using the algorithm proposed by Herraez et al. (2002).

evaluating its argument, thus writing

$$\Delta\phi(\eta, \xi) = \arg(I_F(\eta, \xi)) \,. \tag{2.12}$$

Consequently, the phase difference in equation (2.10) can be estimated by applying this methodology to the reference hologram and to a hologram acquired with a given flow state. This phase difference, however, is only given modulo 2π because of equation (2.12), providing phase difference distributions $\delta\phi$ as illustrated in figure 4(a) which was obtained following this procedure for the two holograms shown in figure 3. In order to correctly estimate OPL variations for tomographic reconstruction, a phase-unwrapping procedure is required to restore continuous 2D phase distributions.

2.3.2. *Phase unwrapping*

Phase map unwrapping aims at restoring a folded phase distribution to its original continuous form, free of 2π jumps. This task can be relatively complex when dealing with noisy data such as holographic phase measurements. In the present case, an additional difficulty is brought by the presence of shock waves in the flow of interest, which naturally induce large phase jumps in some regions of the flow. Various strategies have been proposed in the literature to handle such difficulties (Ghiglia & Pritt 1998). Among the different algorithms available, the one proposed by Herraez et al. (2002) was found to be particularly robust for unwrapping the present phase maps, generally correctly handling the large phase jumps associated with shocks and the phase measurement noise.

An example of application of this unfolding algorithm is shown in figure 4(b), where no obvious unwrapping aberrations can be observed and where phase values around shock waves present sharp transitions. It can be emphasized at this stage that the phase maps obtained provide differential values and that the external region of the flow is considered as the reference region. Consequently, phase maps are automatically adjusted by an additive constant to provide zero phase values on average in this region.

Finally, it should be highlighted that the overall measurement uncertainty of the phase difference $\delta\phi$ obtained after demodulation, filtering and unwrapping is not straightforward to estimate. Future work will have to address this point which requires a dedicated study in itself and which is thus deliberately left aside. It can nonetheless be noted that phase measurement noise should be equal to or greater than the noise observed in the reference holograms, i.e. without flow. With the setup detailed in section 3, it has been estimated to be about 0.15 rad.

2.4. *Resolution*

The Mach–Zehnder interferometric setup presented in figure 2 ensures that the measurement wavefront is planar in the test-section. The holographic image then spatially resolves the flow to the sensor resolution of the camera in the observation plane. However, the spectral filtering process previously discussed degrades the spatial resolution of this phase measurement (Picart et al. 2015). Indeed, equation (2.11) may be written as

$$I_F(\eta,\xi) = I(\eta,\xi) * w(\eta,\xi) \tag{2.13}$$

where $*$ refers to the convolution operator and w is the impulse response of the rectangular filter W applied in the Fourier domain. This impulse response can be expressed in the following form in the observation plane,

$$w(\eta,\xi) = \Delta k_\eta \Delta k_\xi \mathrm{sinc}(\Delta k_\eta \eta)\mathrm{sinc}(\Delta k_\xi \xi) E \tag{2.14}$$

where sinc refers to the normalized sinc function, Δk_η and Δk_ξ are the dimensions of the rectangular window W in the wavenumber plane and $E = \mathrm{e}^{\mathrm{i}(k_{\eta,0}\eta + k_{\xi,0}\xi)}$ with $(k_{\eta,0}, k_{\xi,0})$ the center of the rectangular window. The sinc functions appearing in this kernel will thus spatially smooth the hologram whose resolution will then depend on Δk_η and Δk_ξ. In the present work, the filter size generally covers a quarter of the 2D spectrum as shown in figure 3 and the order of magnitude of the phase measurement spatial resolution in the observation plane is then about 2 pixels.

With the DHI optical setup presented in section 3, given a magnification factor of 0.12, this leads to an estimated spatial resolution for phase measurements of about 100 µm. It is instructive to compare this value with the ones reported in studies relying on tomographic BOS to study similar flows: Nicolas et al. (2017) reported a measurement resolution in the displacement fields of about 2.5 mm and Lanzillotta et al. (2019) improved the BOS optical setup to achieve a spatial resolution of about 0.9 mm. The effect of such differences on the

description of the flow was particularly discussed by Champagnat et al. (2018). While some improvements on these values can certainly be obtained, this discussion emphasizes that DHI more naturally gives a high-resolution description of an object, which is particularly beneficial for the analysis of flows presenting large density variations as in the work of Sugawara et al. (2020). Clearly, this comes at a price of a more complex setup that can only be used for flows of limited spatial extents.

2.5. *Tomographic reconstruction*

With the obtained maps of unwrapped phase difference $\delta\phi$, the variations of OPL can be deduced using equation (2.4). It then remains to solve the inverse problem of estimating the density field $\rho(\boldsymbol{x})$ from a set of line integrals (2.3), obtained simultaneously at different projection angles. An important aspect of DHI is that the light rays probing the volume of interest are parallel, thus permitting the treatment of this tomographic reconstruction problem slice by slice along the jet axis, as in X-ray computed tomography. The projection operator to be considered thus corresponds to the well-known 2D Radon Transform. This is in contrast to BOS tomography (Nicolas et al. 2016; Grauer et al. 2018), where the entire volume must be considered in the inverse problem which involves 3D light ray deviations, making the inference process more computationally challenging. †

Considering a slice of the probed volume, a solution to this inverse problem is sought by discretizing it on a cartesian grid with $M \times M$ square elements of constant density. The discretized measurement model (2.3) in matrix form can then be expressed as

$$\boldsymbol{T}_\theta \boldsymbol{\chi} = \boldsymbol{b}_\theta \tag{2.15}$$

where matrix $\boldsymbol{T}_\theta \in \mathbb{R}^{M\times M^2}$ refers to the discrete projection operator performing integration along the paths followed by the light rays at the projection angle θ, $\boldsymbol{\chi} = (\boldsymbol{\rho} - \rho_0) \in \mathbb{R}^{M^2}$ is the 2D field of density difference in the considered slice rearranged in a (uni-column) vector and $\boldsymbol{b}_\theta \in \mathbb{R}^M$ is the vector gathering the observed variations in optical phase at the observation angle θ. Considering now N_θ projection angles $\{\theta_i\}_{[1..N_\theta]}$, the global linear inverse problem in matrix form may be written as

$$\boldsymbol{T}\boldsymbol{\chi} = \boldsymbol{b} \tag{2.16}$$

with $\boldsymbol{T} \in \mathbb{R}^{MN_\theta\times M^2}$ and $\boldsymbol{b} \in \mathbb{R}^{MN_\theta}$, where the N_θ observed projections are stacked in a single vector. This vector $\boldsymbol{b}$ can be viewed as a flatten sinogram.

One major difficulty hindering a direct resolution of this problem is that $\boldsymbol{T}$ is ill-conditioned because of the sparsity of the projections (the lower the number of projections, the larger the condition number of $\boldsymbol{T}$) and the smoothing action of the measurement process given by equation (2.3) implying that measurement noise naturally present in the projections can significantly corrupt the solution. Various strategies have been proposed in the literature to handle these problems. The two main families of reconstruction methods are the analytical (Fourier methods, Filtered Back-Projection, ...) and the regularized approaches. The latter are of interest in the context of this work for two main reasons: first, they provide a way to distill prior knowledge about the solution and, second, efficient solving methods have been proposed in the literature.

In a Bayesian framework, regularized methods provide Maximum A Posteriori (MAP) solutions in which a measurement noise model is naturally taken into account and where $\boldsymbol{\chi}$

† It can nonetheless be noted that when considering mean axisymmetric flows, dedicated approaches (Xiong et al. 2020) such as the inverse Abel transform and its generalization accounting for non-parallel light rays (Sipkens et al. 2021) can be considered for BOS tomography at a reduced numerical cost.

is considered as a random process. Formally, the problem amounts to solving

$$\underset{\chi}{\operatorname{argmin}} \{\mathcal{F}(\boldsymbol{T}\boldsymbol{\chi} - \boldsymbol{b}) + \mu\,\mathcal{G}(\boldsymbol{\chi})\} \tag{2.17}$$

using an optimization procedure. The first term of this compound criterion provides a measure of data fidelity assuming a measurement noise model while the second one is a regularization term driving the solution under a priori physically-plausible constraints. Here, μ is the regularization parameter and $\mathcal{G}(\cdot)$ is a regularization function. In the following, a least-squares data model is considered, such that $\mathcal{F}(\cdot) = \frac{1}{2}||\cdot||_2^2$. This corresponds to the assumption of a normally distributed measurement noise. This hypothesis has been validated based on the analysis of a series of unfolded reference interferograms and should be approximately valid for averaged phase measurements in the presence of flow. Indeed, unlike DHI applied to opaque surfaces, no speckle noise is present in the holograms. Regarding the regularization term, various functions have been proposed in the literature depending on the type of problem to be solved. To enforce the smoothness of the solution, a Tikhonov (or ℓ_2) regularization approach (Tikhonov & Arsenin 1977) can be used, as chosen by Nicolas et al. (2016) for example for BOS tomography on hot jets and plumes. In the present study, however, a supersonic flow featuring shock waves and thus sharp density gradients is considered. As a consequence, an approach relying on (isotropic) Total Variation (TV) was selected instead to best capture discontinuities in the estimated solution, such that $\mathcal{G}(\cdot) = \mathrm{TV}(\cdot) = ||\nabla \cdot||_1$.

Since TV regularization introduces a non-differentiable function, a different framework than the classical gradient descent approach in the optimization procedure is required and can be found in proximal splitting methods (Chambolle & Pock 2016). In the present work, this optimization problem is solved relying on FISTA (fast iterative shrinkage-thresholding algorithm) (Beck & Teboulle 2009) with a Primal-Dual TV algorithm (Chambolle & Pock 2010) for the regularization problem. Such an approach can be easily followed using open-source codes such as ASTRA-Toolbox (van Aarle et al. 2015) and ToMoBAR (Kazantsev 2019).

The choice of the regularization parameter μ is performed using an L-curve method (Idier 2010), where the regularization term is plotted as a function of the data-fidelity term in log-log scales for various values of μ. As discussed by Hansen (1999) for ℓ_2 regularization problems, a satisfactory compromise may be expected for values of μ where a change of slope is observed in this graph, or equivalently, when the graph curvature κ is maximum. While acknowledging that this simple heuristic approach may be limited in certain cases of study, it has been observed in the present work (where TV regularization is used) that it provides satisfactory estimates of μ with a slight tendency to give under-regularized solutions. This heuristic approach has been used because the exact level of measurement noise is unknown, precluding the use of estimation methods based on the discrepancy principle for example (Hansen 1998). It can furthermore be underlined that the regularization parameter μ will depend on the choice of regularization function but also significantly on the amount of measurement noise.

Finally, this tomographic reconstruction process is probably the main source of uncertainty in the estimated density fields. The subject of uncertainty estimation in tomographic reconstruction is, however, very complex and not settled, requiring a dedicated study out of the scope of the present work. Therefore, no definite confidence intervals can be proposed. Nevertheless, given the results discussed in section 4.1.2, it is reasonable to expect that in the present work the uncertainty in the density estimates could be better than ±5% overall. This level of uncertainty is relatively arbitrary, however, and further work is needed to provide objective values.

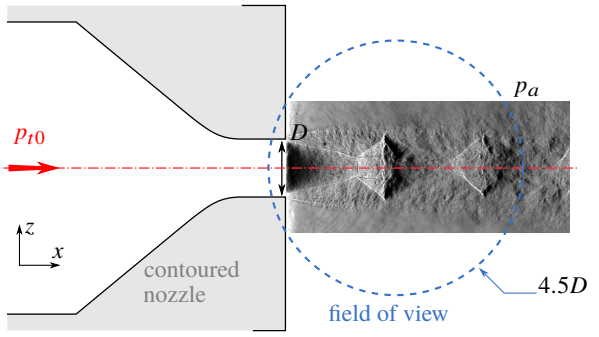


Figure 5: Schematic of the nozzle geometry issuing an under-expanded supersonic jet. The field of view observed by DHI is represented using a blue dashed circle that has an approximate diameter of $4.5D$ where D is the nozzle exit diameter.

3. Experimental setup for multi-view DHI on a screeching supersonic jet

3.1. *Under-expanded jet setup*

The jet facility used is similar to the one described by Nicolas et al. (2017) and Lanzillotta et al. (2019). As illustrated in figure 5, it comprises a contoured, converging nozzle with an inner diameter $D = 22\,\text{mm}$. This nozzle shape ensures a choked condition at the exit. This flush-mounted nozzle is placed in the middle of a $400\,\text{mm} \times 400\,\text{mm}$ metallic panel, providing an extremely thick lip nozzle configuration. The exhausted air is regulated in mass-flow rate and total temperature, with the former maintained at $T_{t0} = 293\,\text{K}$ throughout the experiments. The NPR was monitored using a total pressure probe located $32D$ upstream of the convergent nozzle. In the present work, only one aerodynamic condition given by NPR = 5 is discussed. This value corresponds to an ideally expanded Mach number $M_j = 1.71$ and provides a jet sustaining a helical screech mode C as reported by Lanzillotta et al. (2019) with the present jet facility. Finally, the Reynolds number of the jet based on ideally-expanded values is $\text{Re}_j = U_j \rho_j D_j / \mu_j \approx 1.8 \times 10^6$ with $\rho_j \approx 1.89\,\text{kg m}^{-3}$.

3.2. *Synchronized multi-view DHI setup*

The Mach–Zehnder interferometer presented in section 2.2 was designed taking into account the size of the flow of interest. As illustrated in figure 5, the measurement area extends over a few jet diameters. Given the available volume around the jet and the size and cost of the required optics, an optical setup based on concave mirrors instead of spherical lenses was chosen. A schematic of this Mach–Zehnder interferometer is provided in figure 6, illustrating the paths of the reference and measurement waves. In this optical setup, the concave mirrors have a diameter of 100 mm and a focal length of 1 m. A compact arrangement is obtained by folding the optical path of the measurement wave using flat mirrors between the beam-splitters and the concave mirrors. These concave mirrors are combined with spherical lenses to form two afocal systems. The one in front the camera has a lens of 120 mm focal length, giving an imaging magnification factor of 0.12. This setup was used to obtain the 2D results previously presented in section 2.

A multi-view DHI setup was then obtained by repeating this optical layout by rotational symmetry around the jet axis. As mentioned in section 2.5, the number of projections and their angular distribution are important for the accuracy of the tomographic reconstruction process. Studies on the effects induced by these parameters for tomographic BOS have been reported by Nicolas et al. (2016) and Lang et al. (2017). The conclusions drawn in these studies are expected to be relevant for the present work since closely related tomographic

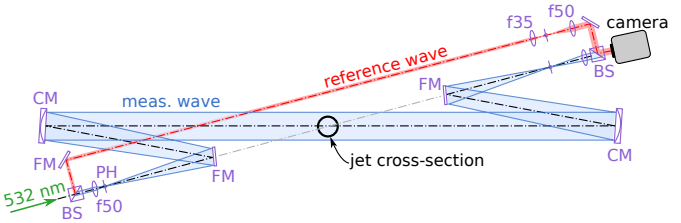


Figure 6: Schematic of one DHI line used to study an under-expanded supersonic jet. In this Mach–Zehnder interferometer, the reference wave is depicted in red and the measurement beam is shown in blue. BS: Beam splitter, PH: pin-hole, FM: flat mirror, CM: concave mirror.

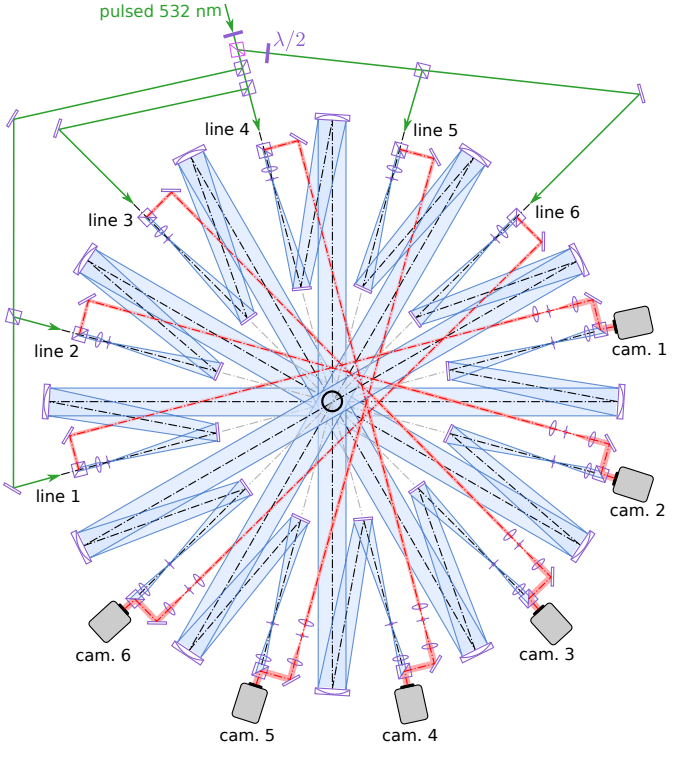


Figure 7: Schematic of the complete optical setup used for multi-view DHI. This setup is composed of 6 Mach–Zehnder interferometers similar to the one displayed in figure 6, centered on the nozzle exit and arranged every 30°.

tools are used. The latter authors particularly highlighted the performance of reconstruction of an axisymmetric density field with cameras evenly distributed on a half-circle or on a full circle, for an even or odd number of projections. Of interest for the present work, it was shown that for such a simplified density field and for a reduced number of cameras (lower than 8), the best results were obtained with an odd number of cameras distributed on a full circle or with cameras distributed on a half-circle. Furthermore, as expected, the larger the number of projections, the more accurate the reconstructions, with a minimum number of projections around 8 before reaching marginal improvements with a half-circle distribution.

In the present work, the guidelines provided by these studies could not be followed because of the bulk of each Mach–Zehnder interferometer. Only 6 lines could be fitted around the

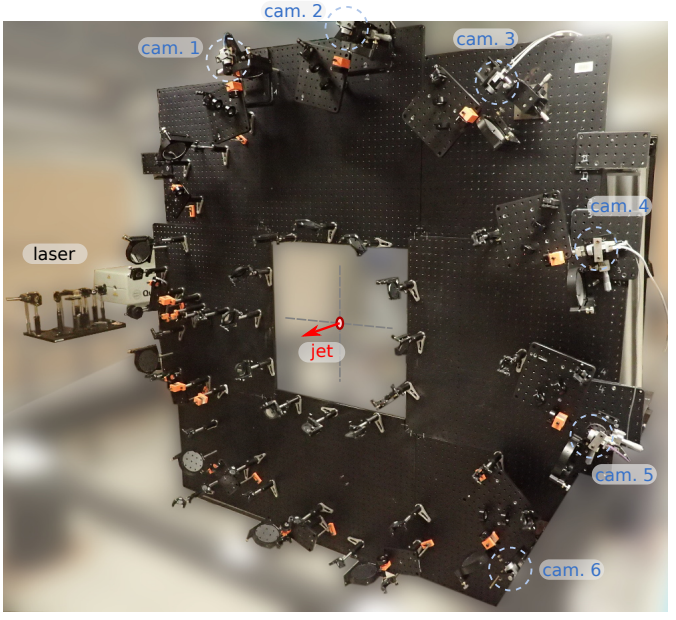


Figure 8: Photograph of the multi-view DHI setup vertically installed around the panel issuing the under-expanded jet.

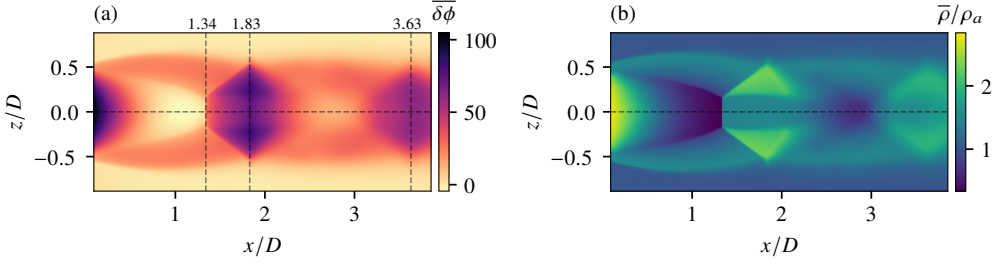


Figure 9: (a) Map of mean unwrapped optical phase $\overline{\delta\phi}$ measured on a choked under-expanded jet at NPR = 5 using the multi-view DHI setup and (b) the mean density ratio $\overline{\rho}/\rho_a$ deduced by axisymmetric tomographic reconstruction, with ρ_a the density of the quiescent atmosphere.

jet on a half-circle, every 30°, as depicted in figure 7. Such a number of projections is relatively small and artifacts limiting the accuracy of the reconstructed density fields are then generally to be expected with direct reconstructions, i.e. without providing additional prior knowledge about the flow topology. This is illustrated for example by Olchewsky et al. (2018) with non-axisymmetric helium jets and ℓ_2 regularization. Nonetheless, this optical layout is perfectly suited to investigate the azimuthal structure of a flow mainly characterized by a reduced azimuthal wavenumber content since it offers a direct means to perform azimuthal Fourier decomposition of the observed projections. This approach is particularly leveraged in section 4 to study the main dynamical structure of the present under-expanded jet.

The practical realization of this multi-view DHI setup is shown in figure 8. Once built horizontally on optical boards, it was re-assembled vertically around the jet nozzle exit on four pneumatic isolators to reduce system vibration. The laser source used was a pulsed Nd:YAG laser (Quanta-Ray Lab-170-10, Spectra Physics) lasing at $\lambda = 532$ nm and equipped

with an injection seeder, providing a coherence length of about 3 m and enhanced output energy stability. It was triggered using a pulsed generator also synchronizing the cameras at a frequency of 10 Hz. In order to balance the amount of energy distributed in each holographic line, the laser beam was successively divided using polarized splitter cubes as shown in figure 7. It can be noted here that this azimuthally-distributed optical layout resembles the one designed by Ishino et al. (2015) to quantitatively study the 3D structure of premixed turbulent flames using 20 synchronized projections. However, these authors relied on schlieren visualization lines that are simpler to setup than DHI lines but that also arguably provide less accurate quantitative measurements.

3.3. *Holograms recording*

The digital holograms were recorded using a set of 6 digital cameras (Basler ace U) equipped with a 1920 px × 1200 px CMOS sensor with pixel size of 5.86 µm. Before performing acquisition at the selected NPR, a series of reference holograms was recorded without flow. Then, three series of 300 digital holograms of the jet were acquired by each camera synchronized on the laser trigger signal at 10 Hz, with continuous operation of the jet facility. Therefore, a total of 900 holograms were obtained for each DHI line.

4. Results and analysis

The optical phase measurements obtained by the multi-view DHI setup on an under-expanded jet at NPR = 5 are analyzed in the following sections. First, the average optical phase and density fields are presented in section 4.1. Then, the main coherent structures associated with the measured optical phase variations are extracted by azimuthal Fourier decomposition and snapshot Proper Orthogonal Decomposition (POD) in section 4.2.

4.1. *Mean density reconstruction*

4.1.1. *Mean optical phase map*

The jet flow being axisymmetric, the map of mean optical phase $\overline{\delta\phi}$ is evaluated by ensemble and azimuthal averaging of 854 instantaneous maps acquired with the 6 holographic lines. This operation thus provides the mean zeroth order azimuthal Fourier mode. The number of instantaneous optical phase maps considered is slightly reduced compared to the total number of acquired snapshots since some outliers for which the optical phase maps were not correctly unwrapped were discarded.

The resulting map is displayed in figure 9(a). In this figure, three particular axial locations are highlighted. First, the Mach disk is estimated to be located around $x = 1.34D$. This value is in agreement with estimates reported by Addy (1981) and Nicolas et al. (2017) for a contoured converging nozzle. Similarly, a matching estimate of $0.35D$ for the Mach disk diameter is obtained. Second, the axial locations of the tips of the first two shock-cells are evaluated to be around $1.83D$ and $3.63D$, providing a shock-cell spacing of about $1.8D$. Again, this estimate is consistent with the value generally obtained with choked jets at such a pressure ratio (Davies & Oldfield 1962; Powell 2010). The mean structure of the present choked under-expanded jet thus appears to be consistent with results reported in the literature.

4.1.2. *Mean density field*

By construction, the mean optical phase map in figure 9(a) displays perfect reflection symmetry across the horizontal axis. As shown in figure 9(b), tomographic reconstruction of the associated density field using the methodology outlined in section 2.5 was then performed accordingly, assuming exact axisymmetry. This is achieved by considering slices of mean

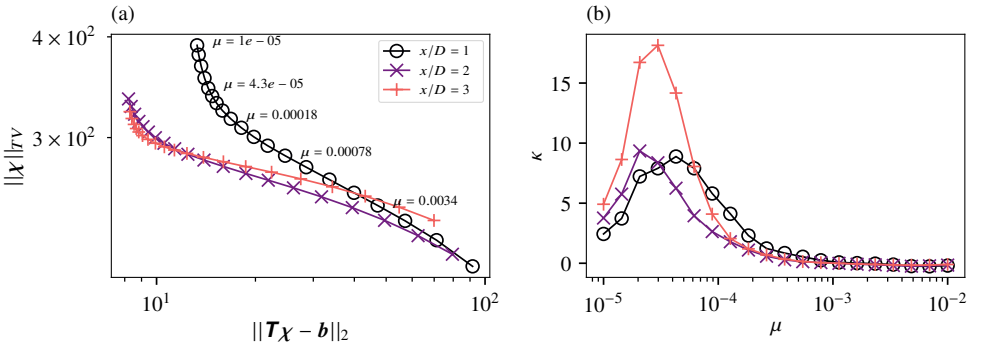


Figure 10: (a) L-curves $\log(||\chi||_{\mathrm{TV}}) = f(\log(||\boldsymbol{T}\chi - \boldsymbol{b}||_2))$ obtained at three axial locations $x/D \in \{1, 2, 3\}$ for a logarithmically-varying regularization parameter μ in the reconstruction process of the mean density field $\overline{\rho}$; (b) the corresponding (log-log) graph curvature curves $\kappa(\mu)$ with $\kappa = f''/(1 + f'^2)^{3/2}$.

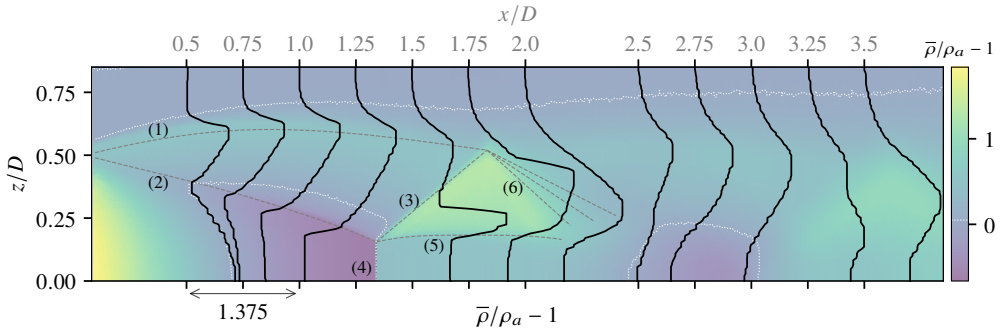


Figure 11: (——) Radial profiles of mean relative density ratio $\overline{\rho}/\rho_a - 1$ obtained by axisymmetric tomographic reconstruction at various axial locations x/D overlayed on the map of mean density ratio shown in figure 9(b). ρ_a refers to the ambient density. Each density profile has its origin horizontally shifted to coincide with the axial location of the slice in the mean density map displayed in the background. The scale of these profiles is given by the double-headed arrow along the x-axis. For conversion purpose, $\rho_j/\rho_a \approx 1.55$. The white dotted lines provide iso-contours of $\overline{\rho}/\rho_a - 1$ at a level of 0.05.

optical phase $\overline{\delta\phi}$ at all axial locations x/D as input data for the tomographic process where it was chosen to use 64 repeated projections evenly distributed on half a circle. It can be noted that a more conventional approach relying on the inverse Abel transform could have been used for this task, as performed by Sugawara et al. (2020) for example. But as emphasized subsequently, the purpose here is to provide validation results for the present tomographic methodology and to discuss the advantages of relying on a regularized tomographic approach.

A suitable value for the regularization parameter μ in equation (2.17) is required for satisfactory density field reconstructions. The L-curve plots and the corresponding (log-log) graph curvature plots $\kappa(\mu)$ obtained for three different slices are displayed in figures 10(a) and 10(b) respectively. These L-curves give clear graph curvature maxima that are obtained for similar values of μ. As a consequence, a single value $\mu = 5 \times 10^{-5}$ was considered for final reconstruction of the mean density field.

A longitudinal cross-section of the reconstructed density field ratio $\overline{\rho}/\rho_a$ is shown in

figure 9(b) and mean relative density profiles $(\overline{\rho} - \rho_a)/\rho_a$ in this (xz)-plane are given in figure 11. The mean density field being axisymmetric, its 3D structure can be easily pictured, particularly up to the first shock-cell which appears to be very stable in time. Following the discussion provided by Panda & Seasholtz (1999) for similar jets, different flow regions have been highlighted in figure 11 using dashed gray lines. The first line labeled (1) indicates approximately the curved boundary of the jet above which one finds the outer mixing layer. The line (2) indicates the presence of a weak shock generated by the coalescence of compression waves. This weak shock delimits the expansion region in the jet core and is known as the barrel shock or the intercepting shock. This expansion ends with a normal shock wave, before which the density falls well below the ambient one, forming the Mach disk identified by (4). From the point of intersection of the Mach disk and the barrel shock (known as the triple-point) emanates a reflected shock labeled (3) and an embedded shear layer (5) which delimits a subsonic region downstream of the Mach disk and a supersonic flow region downstream of the reflected shock wave (3). As expected, a density larger than the ambient one (and than ρ_j) is found between this slip stream (5) and the reflected shock (3). The reflected shock (3) then intersects the external shear layer, giving rise to an expansion fan (6) which closes the first shock cell. Further downstream, a second expansion thus appears leading to a second, more diffuse shock-cell. The structure of this density field and the density levels found appear to be in satisfactory agreement with the measurements obtained by Panda & Seasholtz (1999) using Rayleigh scattering for jets at slightly lower and higher Mach numbers, i.e. $M_j = 1.6$ and 1.8 respectively.

As displayed in figure 11, the density profiles are slightly staggered, which is a direct consequence of the use of TV regularization since it promotes solutions for which $\nabla\boldsymbol{\rho}$ is sparse. Although it can then be expected that the resulting density levels are not perfectly accurate, this drawback is compensated by a satisfactory capture of density jumps across the shock waves present in the flow. Particularly, it can be highlighted that a sharp density jump across the reflected shock (3) is captured (see figure 11, $x/D = 1.5$). It is interesting to note that, for comparison, Sugawara et al. (2020) did not retrieve such a feature in their case of study, probably because of their reconstruction process based on inverse Abel transform. Similarly, sharper density jumps across the embedded annular shear layer are obtained with a progressive thickening in the streamwise direction. As observed in figures 9(b) and 11, a second advantage over other tomographic reconstruction approaches is the absence of numerical artifacts in regions of uniform density such as the external region of the jet or within its core.

Finally, a quantitative comparison of the mean density ratio $\overline{\rho}/\rho_j$ estimated along the jet axis with other measurements reported in the literature is provided in figure 12. The present DHI results are displayed with a ±5% band to quantitatively illustrate the data dispersion associated with such an arbitrary but plausible uncertainty level. First, compared to tomographic BOS results obtained by Nicolas et al. (2017), similar density levels are observed but with a better capture of the density profile across the Mach disk. Indeed, tomographic BOS results probably suffer from a larger spatial resolution associated with the BOS optical setup and a more complex tomographic reconstruction process relying on a ℓ_2 regularization which probably oversmooths the gradients. Second, compared to the density profile obtained by Panda & Seasholtz (1999) at a higher Mach number $M_j = 1.8$ (NPR ≈ 5.75), a very similar shape is obtained, supporting the relevance of the reconstructed field. In the present case, the location of the Mach disk is closer to the jet exit plane and larger density levels (close to ρ_j) in the shock-cell regions are measured. This is expected since the higher the Mach number, the greater the excessive heating due to non-isentropic compression associated with the normal shock wave and thus the lower the density in these regions. Finally, it can be highlighted that the density profile measured after the first Mach

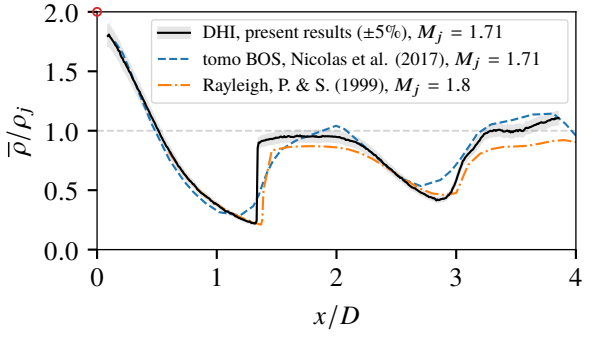


Figure 12: Mean density ratio $\overline{\rho}/\rho_j$ along the jet axis at NPR = 5 (M_j = 1.71) obtained with the present experimental apparatus (DHI) and with tomographic BOS (Nicolas et al. 2017), with ρ_j the fully-expanded isentropic jet density. The axial profile measured by Panda & Seasholtz (1999) using Rayleigh scattering at M_j = 1.8 is also given for qualitative comparison purpose. The isentropic value at the nozzle exit is given by a red circle (○).

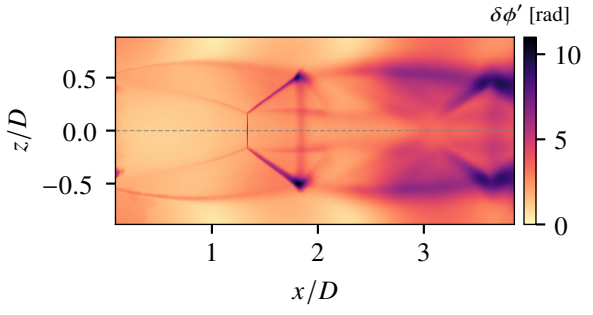


Figure 13: Map of root mean square values of temporal optical phase fluctuations $\delta\phi' = \mathrm{rms}(\widetilde{\delta\phi})$.

disk is relatively flat, showing a plateau value over an extent in the streamwise direction corresponding to the internal subsonic region delimited by the embedded axisymmetric shear layer (from $x/D \approx 1.34$ to $x/D \approx 2$). A slightly different behavior is observed in the second shock-cell, with a progressive increase in density ($x/D \approx 3.5$), in agreement with the measurements reported by Panda & Seasholtz (1999).

4.2. *Identification of the main coherent structures*

While the previous mean-field analysis mainly focused on axisymmetric results for which only a single holographic line could have been used, a methodology exploiting the simultaneity of the acquisitions obtained with the 6 holographic lines is now discussed, with the objective of identifying the main coherent azimuthal structure of the fluctuating density field.

4.2.1. *Phase fluctuation map*

An instantaneous optical phase distribution obtained with one holographic line can be decomposed into a mean component $\overline{\delta\phi}$, discussed in the previous section 4.1, and a fluctuating component $\widetilde{\delta\phi}$, such that

$$\delta\phi(t,\eta,\xi,\theta_k) = \overline{\delta\phi}(\eta,\xi,\theta_k) + \widetilde{\delta\phi}(t,\eta,\xi,\theta_k)\,, \tag{4.1}$$

where t refers to a discrete time, (η, ξ) to the coordinates in the observation space and θ_k to the k^{th} projection angle. Similarly, an instantaneous 3D density field ρ is decomposed into a mean field $\overline{\rho}$ and a fluctuating field $\widetilde{\rho}$, writing

$$\rho(t, x, y, z) = \overline{\rho}(x, y, z) + \widetilde{\rho}(t, x, y, z)\,, \tag{4.2}$$

where (x, y, z) are the coordinates in physical space. By linearity of the operators in (2.3) and (2.4), the two optical phase terms $\overline{\delta\phi}$ and $\widetilde{\delta\phi}$ are the projected results at an angle θ_k of $\overline{\rho}$ and $\widetilde{\rho}$ respectively. Analyzing the statistical properties of $\widetilde{\delta\phi}$ thus provides information on the structure of $\widetilde{\rho}$.

The azimuthally-averaged field of root mean square (rms) values of $\widetilde{\delta\phi}$, referred to as $\delta\phi'$, is shown in figure 13 and highlights the projected regions of the flow with intense density variations. The reflected shock wave in the first shock cell appears to sustain some local but intense fluctuations, particularly at the junction with the external shear layer. Downstream, significant fluctuations in the jet shear layer and in the second shock-cell can also be observed, as well as in the embedded shear layers to a lesser extent. Finally, this figure shows the well-known presence of a spatially-stationary wave envelope outside the jet shear layer, which is the interfering result of downstream and upstream propagating waves that are building blocks in the screech feedback mechanism (Panda & Seasholtz 1999; Edgington-Mitchell 2019). The resulting wave is generally referred to as the jet near-field "standing wave".

4.2.2. *Azimuthal structure of the observed projections*

As previously emphasized, the 6-view DHI setup was designed to provide instantaneous optical phase maps with observation lines regularly distributed in the jet azimuthal direction, for projection angles $\theta_k \in \{0°, 30°, ..., 150°\}$. Since the observed optical phases result from integration through the entire flow field, an augmented observation state for the optical phase fluctuations can be constructed by rotational symmetry around the jet axis, such that

$$\widetilde{\delta\phi}^{a}(t, \eta, \xi, \theta_k) = \widetilde{\delta\phi}(t, \eta, \xi, \theta_k) \tag{4.3}$$

$$\widetilde{\delta\phi}^{a}(t, \eta, \xi, \theta_k + 180°) = \widetilde{\delta\phi}(t, \eta, -\xi, \theta_k)\,. \tag{4.4}$$

This augmented observation state is then defined for projection angles homogeneously distributed all around the jet, every 30°, and can be decomposed into azimuthal Fourier modes $\widehat{\delta\phi}^{a}_{m}$ with azimuthal wavenumbers $m \in \{-N_\theta, ..., N_\theta - 1\}$, writing

$$\widetilde{\delta\phi}^{a}(t, \eta, \xi, \theta_k) = \frac{1}{2N_\theta} \sum_{m=-N_\theta}^{N_\theta-1} \widehat{\delta\phi}^{a}_{m}(t, \eta, \xi) \mathrm{e}^{\mathrm{i}m\theta_k}\,, \tag{4.5}$$

where $N_\theta = 6$ in the present study. The instantaneous and average azimuthal structure of optical phase fluctuations can then be obtained, providing insights into the azimuthal structure of the flow density field.

The azimuthal mean energy distribution of the optical phase fluctuations is assessed by considering mean square values of the azimuthal Fourier modes amplitudes $|\widehat{\delta\phi}^{a}_{m}|$. Indeed, time-averaging Parseval's relation allows to define a mean distribution of azimuthal optical phase fluctuation energy $\overline{E}_\theta(\eta, \xi)$ such that

$$\overline{E}_\theta = \sum_{k=0}^{2N_\theta-1} \mathrm{var}(\widetilde{\delta\phi}^{a}(t, \theta_k)) = \frac{1}{2N_\theta} \sum_{m=-N_\theta}^{N_\theta-1} \langle |\widehat{\delta\phi}^{a}_{m}(t)|^2 \rangle\,, \tag{4.6}$$

where $\langle\cdot\rangle$ refers to the ensemble mean, $\mathrm{var}(\cdot)$ to the variance operator along the time dimension and where the coordinates in the observation space have been omitted for clarity. The maps

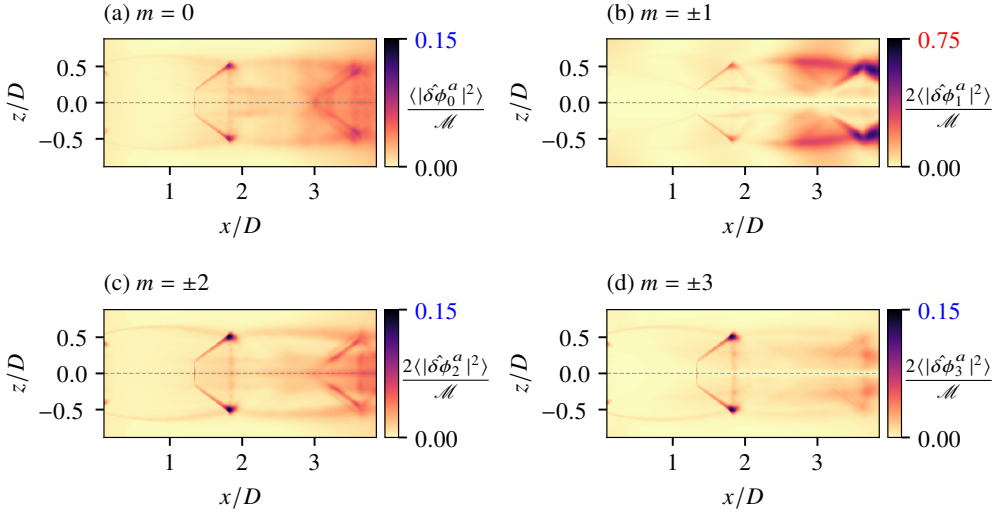


Figure 14: Maps of relative energy distribution in the first four azimuthal Fourier modes of observed optical phase fluctuations. For clarity only, the aerodynamic frame is used instead of the observation one. The normalization term is $\mathscr{M} = \max(2N_\theta \overline{E}_\theta)$, see equation (4.6). As emphasized using colored labels, figure (b) displaying results for the azimuthal wavenumber $m = \pm 1$ features maximum values five times larger compared to figures (a,c,d).

of normalized values of $\langle|\widehat{\delta\phi}_m^a(t)|^2\rangle$ are displayed in figures 14(a–d) for four azimuthal wavenumbers, the remaining modes having low energy content. Relying on equation (4.6), the normalization term used is $\mathscr{M} = \max(2N_\theta \overline{E}_\theta)$, permitting the identification of regions in the azimuthal Fourier modes contributing the most to the observed optical phase fluctuations. It is emphasized that in these figures, the contributions of positive and negative azimuthal wavenumbers $\pm m$ are summed, resulting in a factor of 2 on the maps of non-axisymmetric modes ($m > 0$) since $\widehat{\delta\phi}_{\pm m}^a$ are complex conjugates. Figure 14(b) highlights that most of the optical phase fluctuations are associated with the $m = \pm 1$ helical modes, with local values reaching up to 75% of the observed maximum mean optical phase fluctuation energy. These large fluctuations are identified in the region of the flow where the second shock-cell interacts with the external jet shear layer. Significant fluctuations are also present upstream, in the outer shear layer found between the two shock-cells and in the reflected shock of the first cell. As displayed in figures 14(a,c,d), the other azimuthal modes have about five times smaller maximum fluctuation energy amplitudes. Interestingly, all of these azimuthal modes capture significant fluctuations in the oblique shock of the first shock-cell, particularly in the region where it intersects the external shear layer. This suggests that shock oscillation in the first shock-cell cannot be explained primarily by the dynamics of a single pair of azimuthal modes, in contrast to the second shock-cell whose motion appears to be largely driven by the first helical modes $m = \pm 1$.

The dominance of the first pair of helical modes is made more evident in figure 15 which provides a measure of the relative magnitudes of the total energy contained in the maps $\langle|\widehat{\delta\phi}_m^a|^2\rangle$ using the Frobenius norm denoted by $||\cdot||_F$. While the first pair of helical modes at $m = \pm 1$ provides about 58% of the total energy, the other azimuthal modes all have contributions less than 10%.

Finally, the map of rms values of optical phase fluctuations $\delta\phi'$ previously shown in

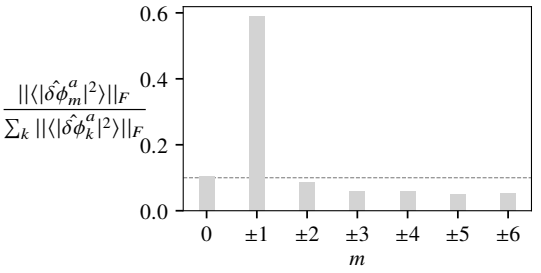


Figure 15: Relative magnitudes of phase fluctuation energy contained in the 2D maps of mean square azimuthal Fourier modes amplitudes $\langle|\widehat{\delta\phi}^a_m|^2\rangle$ as a function of the azimuthal wavenumber m, with summed contributions for complex conjugate pairs.

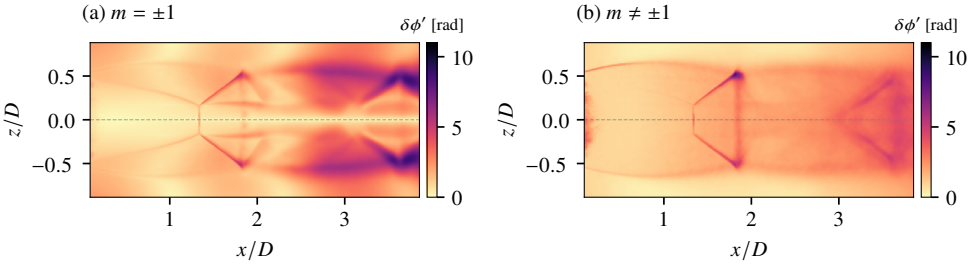


Figure 16: Maps of rms values of temporal optical phase fluctuations $\delta\phi'$ obtained (a) by isolating the contributions of the first pair of complex-conjugate azimuthal modes ($m = \pm 1$) and (b) by considering the contributions of all the other azimuthal modes ($m \neq \pm 1$).

figure 13 is decomposed in figures 16(a,b) by respectively isolating and discarding the contributions of the first pair of helical modes. As observed in figure 16(a), the dominant pair of azimuthal modes at $m = \pm 1$ captures the footprint of the standing wave present in the external near-field of the jet, this feature being almost totally absent from the map associated with the remaining modes in figure 16(b). As previously stated, this standing wave can be associated with the screech feedback loop. This observation, along with the large optical phase fluctuations observed, suggest that the salient features of screech mode C characterized by a helical instability wave are captured by the present azimuthally-filtered measurements.

4.2.3. *Proper Orthogonal Decomposition of the dominant helical Fourier mode*

The previous azimuthal Fourier decomposition provided insights into the time-average azimuthal energy distribution of the observed optical phase fluctuations, highlighting that screech-related dynamical structures were embedded in the isolated complex-conjugate modes at $m = \pm 1$. Yet, because of the unsteady nature of the system, which is furthermore only observed at discrete and distant time intervals, exposing an average 3D density picture of these structures is not straightforward.

In this work, it is proposed to rely on Proper Orthogonal Decomposition (POD) (Holmes et al. 2012) to efficiently isolate these coherent structures and to provide a simple modeling framework for their dynamics. POD aims at decomposing an ensemble of space-time-varying fields $\{f(t_j, \boldsymbol{x})\}_{j=1..P}$ into a linear combination of spatial orthogonal modes $\Psi_i^{(f)}(\boldsymbol{x})$ optimally capturing its temporal variance or energy. Here, $\boldsymbol{x} \in \mathbb{R}^3$ refers to spatial coordinates

in the frame of interest, which can be in the physical or in the observation space. It is emphasized that f is considered in this work as a zero-mean complex-valued function and that, consequently, the spatial modes are also complex. The decomposition writes

$$f(t_j, \boldsymbol{x}) = \sum_{i=1}^{P} a_i(t_j) \Psi_i^{(f)}(\boldsymbol{x}), \tag{4.7}$$

with $a_i(t_j)$ the discrete temporal complex coefficients animating the spatial modes. In discrete form, data functions and spatial modes are replaced by N_{xyz}-vectors, with N_{xyz} the number of spatial points considered, such that equation (4.7) may be written as

$$\boldsymbol{f}_j = \sum_{i=1}^{P} a_{i,j} \boldsymbol{\Psi}_i^{(f)}. \tag{4.8}$$

Following Sirovich (1987), when the observations $\{\boldsymbol{f}_j\}$ are independent, this decomposition can be retrieved by considering the eigenvalue problem associated with the $P \times P$ temporal covariance matrix $\boldsymbol{C}^{(f)}$ defined by elements $c_{m,n}^{(f)} = \boldsymbol{f}_n^{\mathrm{H}} \boldsymbol{f}_m / P$ where $\cdot^{\mathrm{H}}$ refers to the conjugate transpose operator. The eigenvectors of $\boldsymbol{C}^{(f)}$ provide the temporal coefficients $a_{i,j}$ and the spatial modes are obtained by linear combination, such that

$$\boldsymbol{\Psi}_i^{(f)} = \sum_{j=1}^{P} a_{i,j} \boldsymbol{f}_j. \tag{4.9}$$

Furthermore, $\boldsymbol{C}^{(f)}$ being Hermitian, its eigenvalues λ_i are real and give the energy associated with the spatial modes $\boldsymbol{\Psi}_i^{(f)}$. This approach is computationally interesting when $P \ll N_{xyz}$ and is commonly referred to as the method of snapshots.

In this work, the P augmented snapshots of optical phase $\widetilde{\delta\phi}^a$ are arranged as QN_θ^a-vectors and stacked in a matrix $\boldsymbol{\Phi} \in \mathbb{R}^{QN_\theta^a \times P}$, with $Q = MN_x$ the number of data points in one phase map and $N_\theta^a = 2N_\theta$ the number of augmented projections. Snapshot POD is then applied to the deduced P maps of helical Fourier modes at $m = 1$ arranged as Q-vectors and stacked to form the snapshot matrix of Fourier modes $\widehat{\boldsymbol{\Phi}}_{m=1} \in \mathbb{C}^{Q \times P}$. The temporal covariance matix then writes $\boldsymbol{C}^{(\phi)} = \widehat{\boldsymbol{\Phi}}_m^{\mathrm{H}} \widehat{\boldsymbol{\Phi}}_m / P$. Solving the associated eigen problem provides the real eigenvalues λ_i and the associated POD modes $\widehat{\boldsymbol{\Psi}}_i^{(\phi)} \in \mathbb{C}^Q$ for $i \in [1..P]$, which can be rearranged to form complex spatial maps of size $M \times N_x$. Selecting a limited number of main modes, an inverse discrete azimuthal Fourier transform may then be applied to obtain an arbitrary number $N'_\theta > N_\theta$ of projections in the observation space of optical phase fluctuations, thus allowing to perform an accurate reconstruction of the associated density fields relying on the tomographic reconstruction approach described in section 2.5.

This way of proceeding to estimate the density field of screech-related spatio-temporal modes is summarized in the flowchart shown in figure 17 using solid black arrows, where azimuthal Fourier transform and snapshot POD are directly performed on the entire set of observations. Other paths may however be imagined and it is important to clarify whether the present process yields main modes similar to those that would be obtained with azimuthal Fourier transform and POD directly applied to snapshots of density fields. Indeed, such an approach may be considered more physically relevant since the decomposition would then be performed in physical space and not in observation space. This way of proceeding is also illustrated in the flowchart shown in figure 17, but using dashed gray arrows. First, the inverse tomographic problem for the ensemble of acquired projections would have to be solved, providing the matrix $\boldsymbol{X} \in \mathbb{R}^{N_{xyz} \times P}$ gathering the P temporal snapshots of 3D fields of

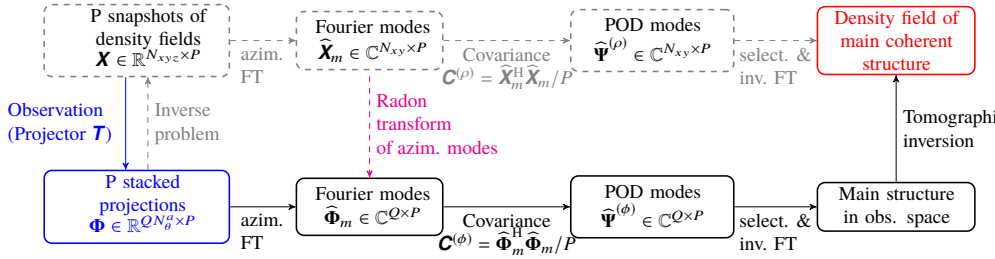


Figure 17: Flowchart illustrating possible approaches to evaluate the main screech-related coherent structures in the observed instantaneous density fields using snapshot POD. The dashed gray path indicates an idealized direct approach where azimuthal Fourier transform (FT) and POD would be performed on the reconstructed 3D density fields snapshots. The solid black path describes the method that was followed in this work. The blue node highlights the starting point, the available observations, which are the sinograms gathering the variations of optical phase for each observation angle. The magenta dashed line indicates the possibility of applying a Radon transform between azimuthal modes.

$\widetilde{\rho}$ obtained on a cartesian grid of size $N_{xyz} = N_x M^2$. An azimuthal Fourier transform would then directly provide the azimuthal Fourier modes $\widehat{\boldsymbol{X}}_m$ and the deduced covariance matrix would be $\boldsymbol{C}^{(\rho)} = \widehat{\boldsymbol{X}}_m^{\mathrm{H}} \widehat{\boldsymbol{X}}_m / P$. Applying an inverse Fourier transform to the selected main POD modes would finally provide the main 3D structures of density fluctuations associated with screech. Clearly, the major drawback with this approach lies in its first step, since it requires tomographic inversion of the entire set of projections. In practice, this represents a non-negligible computational burden and it cannot yield satisfactory results in the present work because of the limited number of available projection angles. Nonetheless, arguments can be provided to support the approximate equivalence of the two paths.

First of all, it is highlighted that Radon and azimuthal Fourier transforms can be intertwined. Indeed, as demonstrated in appendix A, this is the consequence of conservation of azimuthal symmetries by the Radon transform and of its linearity. The azimuthal Fourier modes in the observation space can thus be alternatively obtained writing $\widehat{\boldsymbol{\Phi}}_m = \boldsymbol{T}_m \widehat{\boldsymbol{X}}_m$ where $\boldsymbol{T}_m$ refers to the Radon transform of an azimuthal Fourier mode. This relation is displayed in figure 17 using a magenta arrow. Given this result, the question then actually amounts to knowing if the temporal covariance matrices $\boldsymbol{C}^{(\rho)}$ and $\boldsymbol{C}^{(\phi)}$ provide similar eigenfunctions for the dominant modes. Noting that $\boldsymbol{C}^{(\phi)} = \widehat{\boldsymbol{X}}_m^{\mathrm{H}} (\boldsymbol{T}_m^{\mathrm{H}} \boldsymbol{T}_m) \widehat{\boldsymbol{X}}_m / P$, the two covariance matrices would be similar if the projection operator $\boldsymbol{T}_m$ was orthogonal. This is not the case for the Radon transform and the projection-backprojection pair is known to produce blurred, spectrally-filtered images (Epstein 2008; Paleo 2017). This spectral feature appears for example in the filtered-backprojection approach where a frequency-filter is used to obtain a practical inversion algorithm. $\boldsymbol{T}_m^{\mathrm{H}} \boldsymbol{T}_m$ acts as a low-pass frequency filter in the image domain and thus promotes large-scale density variations in the covariance matrix $\boldsymbol{C}^{(\phi)}$. While a detailed quantitative analysis of this filtering process is out of the scope of the present work, these observations suggest that the main eigenfunctions obtained from $\boldsymbol{C}^{(\phi)}$ and $\boldsymbol{C}^{(\rho)}$ are likely to be similar and the two paths shown in figure 17 should yield comparable modes, thus allowing the main coherent large-scale density structures to be isolated.

4.2.4. *A reduced dynamical model*

Snapshot POD described in the previous section was applied to the $P = 854$ instantaneous Fourier modes of optical phase fluctuations at the main azimuthal wavenumber $m = 1$. The normalized eigenvalues of $\boldsymbol{C}^{(\phi)}$ are shown in figure 18 in descending order and in logarithmic

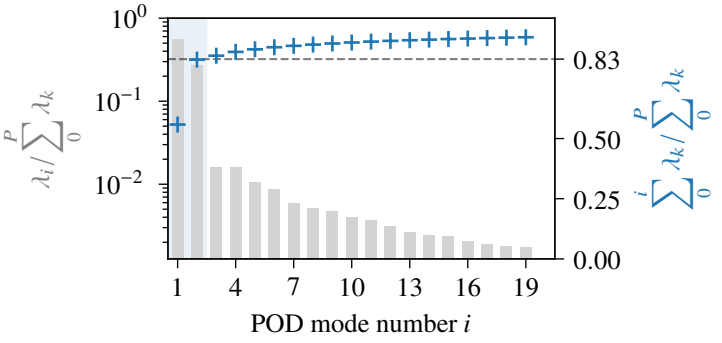


Figure 18: Normalized eigenvalues (vertical gray bars) in logarithmic scale of the temporal covariance matrix $\boldsymbol{C}^{(\phi)}$ deduced from the snapshots of azimuthal Fourier modes at an azimuthal wavenumber $m = 1$, and their cumulative sum (blue cross markers) in linear scale for a reduced number of POD modes.

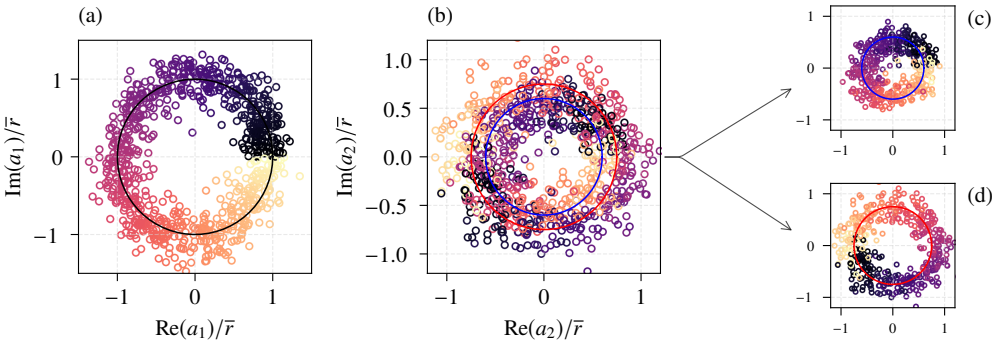


Figure 19: Normalized scatter plots obtained from the collection of the first two complex POD modes coefficients $\{a_i(t_j)\}_{i=1..2}$. Data points are color-coded to highlight phase links across the plots. (a) scatter plot of $\mathrm{Re}(a_1(t_j))/\bar{r}$ and $\mathrm{Im}(a_1(t_j))/\bar{r}$ with $\bar{r}$ a normalizing constant; the markers colors encode the phase of $a_1(t_j)$, noted $\varphi_1(t_j)$; the large black circle represents a model orbit or phase portrait in the phase space the POD mode. (b) scatter plot of $\mathrm{Re}(a_2(t_j))/\bar{r}$ and $\mathrm{Im}(a_2(t_j))/\bar{r}$; markers colors are still a function of $\varphi_1(t_j)$; two different phase portraits are identified and modeled by blue and red circular orbits. (c-d) separated scatter plots deduced from (b) highlighting the two different superposed distributions and the associated modeled orbits.

scale for only a few modes, together with the associated cumulative sum in linear scale. Two POD modes concentrate about 83% of the optical phase fluctuation energy for this azimuthal mode, with the eigenvalues λ_1 and λ_2 being an order of magnitude larger than the others.

To study the phase relationship that may exist between these two main POD modes, scatter plots of the real and imaginary parts of the complex POD mode coefficients $a_1(t_j)$ and $a_2(t_j)$ are displayed in figure 19. First, in figure 19(a), $\mathrm{Im}(a_1(t_j))$ is plotted as a function of $\mathrm{Re}(a_1(t_j))$ using a normalization amplitude $\bar{r}$. The resulting distribution can be described by a circular orbit with radial dispersion, suggesting that the temporal coefficients of the first POD mode embed relatively coherent temporal dynamics subject to amplitude fluctuations. Without considering the observed dispersion, the evolution of amplitude and phase of the first POD mode can then be approximated by a reduced dynamical model $\widetilde{\mathcal{M}}_1$ taking the

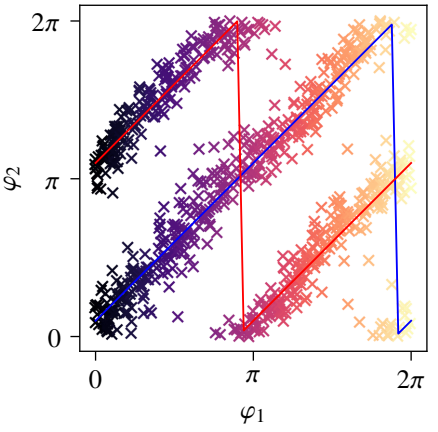


Figure 20: Scatter plot of $\varphi_1(t_j)$ and $\varphi_2(t_j)$, which are the phases of the complex POD modes coefficients $a_1(t_j)$ and $a_2(t_j)$ respectively. The markers are color-coded by φ_1 as in figure 19. The blue and red solid lines represent linear phase relationships modeling the phase links observed in figure 19(b) for the two orbits displayed with the same two colors.

form of a simple harmonic oscillator written as

$$\widehat{\mathcal{M}}_1(t_j, \boldsymbol{x}) = \overline{r}\, \widehat{\Psi}_1^{(\phi)}(\boldsymbol{x})\, \mathrm{e}^{\mathrm{i}\Omega(t_j)} \tag{4.10}$$

where $\widehat{\Psi}_1$ is the first spatial POD mode, $\boldsymbol{x} = (\eta, \xi)$ refers to the spatial coordinates in the observation space and $\Omega(t_j)$ is a real-valued function providing the instantaneous phase of the mode. For example, assuming stationary cyclic dynamics for screech, it could be modeled as $\Omega(t_j) = \pm\omega_s t_j$ with ω_s the screech angular frequency, such that the black orbit shown in figure 19(a) would be followed at constant angular velocity in one direction of rotation or the other.

The second scatter plot shown in figure 19(b) displays $\mathrm{Im}(a_2(t_j))$ as a function of $\mathrm{Re}(a_2(t_j))$, normalized by the same scalar $\overline{r}$ as for the first POD mode coefficient. This graph is more complex to describe and, to facilitate its reading, each data point has been colored according to the instantaneous phase of the first POD mode coefficient, i.e. $\varphi_1(t_j) = \arg(a_1(t_j))$. This color-coding can be observed in figure 19(a). It serves to highlight the phase relationships that exist between the two POD modes and allows for a simple cluster analysis to be performed visually. Two different distributions can be identified in figure 19(b), with more explicit cluster partitions separately drawn in figure 19(c) and figure 19(d). The first distribution highlighted in figure 19(c) shows a collection of points scattered around an approximate circular orbit (displayed in blue), with an average radius around $0.6\overline{r}$ and with markers colors indicating an approximate phase-match with the first POD mode coefficients. The second isolated distribution of points shown in figure 19(d) also describes an approximate circular orbit (drawn in red), but with a larger average radius around $0.75\overline{r}$ and an approximate antiphase relationship with the first POD mode coefficients. Consequently, for one state of the dynamical system described by the first POD mode, two different orbits may be exclusively followed in the phase space of the second POD mode. As shown thereafter, this behavior captures the two possible azimuthal directions of rotation of the helical instability here observed. The probabilities of following either orbit in the phase space of the second POD mode are almost equal ($50\% \pm 0.5\%$), since a similar number of snapshots were found in the scatter plots 19(c) and 19(d). It is concluded that the helical structure subsequently presented has no preferred azimuthal direction of rotation about the

jet axis. Finally, this state decomposition indicates that the studied jet can only support one of the two identified structures over a period of time. More particularly, it is evaluated that the transition probability from one state to the other over the time interval separating two snapshots, i.e. 0.1 s corresponding to about 460 screech cycles, is about 7% for the considered NPR.

This switching in the direction of rotation observed during continuous operation appears to be facility-dependent. For example, Powell et al. (1992) reported that in their experiments "the sense of rotation remained the same during continuous operation of the jet, but was liable to be different when the jet has been turned off and then on again." In the present case, the observed intermittency suggests that the feedback loop has been stochastically perturbed during operation, allowing the dynamical system to switch between the two observed limit cycles. At least two possible mechanisms can be imagined. First, stochastic variations in upstream flow conditions (pressure variations, flow turbulence, ...) could have acted as forcing terms in the jet receptivity process. Second, the present experiment has a significantly larger nozzle lip thickness compared to Powell et al. (1992). This difference in boundary conditions may be of importance since the nozzle lip geometry plays a major role in receptivity and has been shown to have a significant effect on the feedback loop (Raman 1999; Edgington-Mitchell 2019). Although a thicker nozzle lip is known to increase the strength of the screech noise and thus the feedback loop, an increase in the energy of the present stochastic dynamical system could also promote intermittent escapes from the two potential wells in which the two observed limit cycles evolve. Notably, a more stable helical mode has been observed by the present authors with the same jet facility but with part of the nozzle lip covered with acoustic dampening foam. The nature of this intermittency therefore needs to be clarified by complementary experimental studies of these two hypotheses.

The exact phase relationships between the two POD modes for the two possible orbits evidenced in figure 19(b) are made more explicit in figure 20, where the phase of the second POD mode, noted φ_2 is plotted as a function of φ_1. Linear relationships provide satisfactory models for the two observed trends with a phase difference of π. As a consequence, extending the reduced model for the first POD mode given by equation 4.10, a simple linear model describing the main jet dynamics captured by these two POD modes in the azimuthal Fourier domain of the observation space can be proposed using two phase-coupled harmonic oscillators, writing

$$\widehat{\mathcal{M}}^{\pm}(t_j, \boldsymbol{x}) = \bar{r}\left(\widehat{\Psi}_1(\boldsymbol{x}) + c_2^{\pm}\widehat{\Psi}_2(\boldsymbol{x})\, \mathrm{e}^{\mathrm{i}p_2^{\pm}}\right) \mathrm{e}^{\mathrm{i}\Omega(t_j)} \tag{4.11}$$

where $c_2^{\pm}$ and $p_2^{\pm}$ are parameters accounting for the reduced radii and the phase shifts associated with the two circular orbits identified in the phase-space of the second POD mode. Note that the exponent $\cdot^{(\phi)}$ was omitted for clarity. Relying on figure 19 and figure 20, the two orbits are more explicitly described by $c_2^{+} \approx 0.6$ and $p_2^{+} \approx \pi/10$ for the orbit almost in phase with the first POD mode (blue in the figures 19(b) and 19(c)), and $c_2^{-} \approx 0.75$ and $p_2^{-} \approx 11\pi/10$ for the second one associated with antiphase dynamics (red in the figures 19(b) and 19(d)). In the context of dynamical systems theory, this model (4.11) is expected to approximate the attractor of the system whose limit cycle is here described by periodic orbits in POD phase space.

It is highlighted that the observed difference in orbit radii in the phase space of the second POD mode has not found a definite explanation. It has been verified that this result does not depend on the number of snapshots considered and that could have led to covariance convergence issues, nor apparently on the optical setup since halving the number of projections gave similar results. It is conjectured that this difference in the mode amplitudes between the two observed states has a physical origin and actually captures slightly

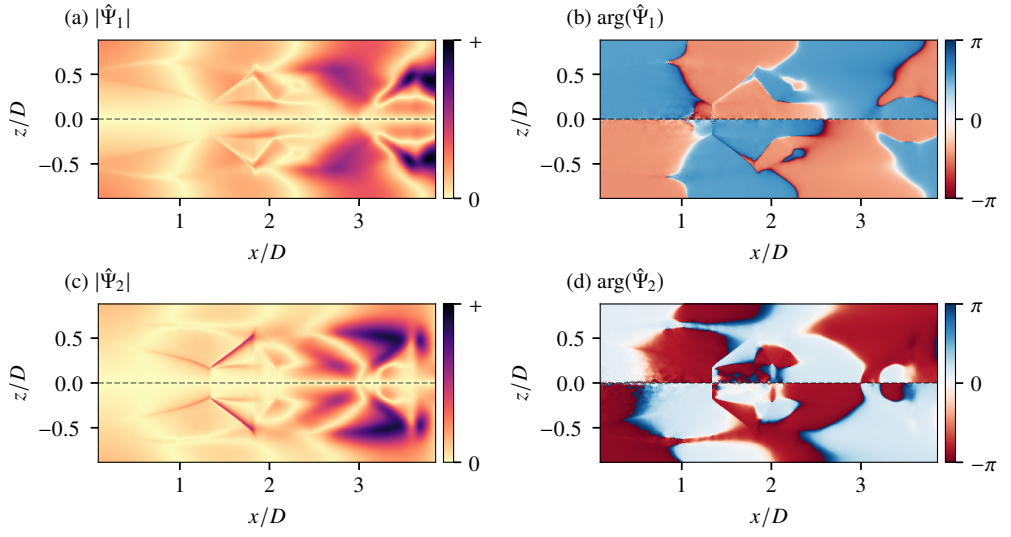


Figure 21: (a, c) Amplitude and (b, d) phase maps of the two main complex POD modes $\widehat{\Psi}_1(\boldsymbol{x})$ and $\widehat{\Psi}_2(\boldsymbol{x})$ identified in the first azimuthal Fourier mode ($m = 1$) of observed instantaneous optical phase fluctuations $\widetilde{\delta\phi}^a$.

different density fluctuations between the two possible azimuthal directions of rotation of the observed helical instability wave. This could be induced by some subtle non-axisymmetric experimental conditions (jet swirl, nozzle geometry, jet surrounding, ...) that could slightly favour the growth of the instability in one azimuthal direction, without significantly favoring the probability of rotation in one of the two directions.

4.2.5. *POD spatial modes and projection in the observation space*

The reduced model proposed in equation (4.11) is composed of two complex spatial modes $\widehat{\Psi}_1$ and $\widehat{\Psi}_2$ in the azimuthal Fourier domain of the observation space. Their spatial structure in terms of amplitude and phase are displayed in figure 21. Focusing first on the amplitudes shown in figures 21(a) and (c), it can be observed that both modes capture coherent optical phase fluctuations in different regions of the jet. For example, $\widehat{\Psi}_1$ captures greater variance downstream and slightly upstream of the second shock-cell, while $\widehat{\Psi}_2$ displays maximum variations in the external shear layer just upstream the second shock-cell and in the reflected shock of the first shock-cell. It may also be noted that both modes embed the footprint of the external stationary wave, but that it is more pronounced in $\widehat{\Psi}_1$. Focusing now on the phase of the two complex modes displayed in figures 21(b) and (d), well-defined patches of approximately constant phase can be observed, providing indications about the spatial coherence of the isolated fluctuations. For both modes, antiphase distributions are obtained with respect to the jet axis, which is expected since the helical mode at $m = 1$ is studied. The first mode exhibits patches of constant phase around $-\pi/2$ and $\pi/2$, while the second mode displays patch values around 0 and $-\pi$, indicating that both modes are in azimuthal phase-quadrature. These observations can be interpreted as follows: taken individually, the two modes $\widehat{\Psi}_1$ and $\widehat{\Psi}_2$ describe purely azimuthal fluctuations at $m = 1$ and are not able to render features such as axial convection or helicity. These can only be rendered in the observed space by streamwise and azimuthal quadrature between two modes, which is a known feature of POD applied to convective instabilities (see for example Oberleithner

et al. (2011), Schmid et al. (2012) and Edgington-Mitchell et al. (2014b) among others). As shown in the following section, summation of the two modes does indeed recover convective structures in the observation space and rotating helical density structures in the physical space.

The reduced model (4.11) is expressed in the azimuthal Fourier domain of the observation space. For the purpose of reconstructing the associated density field, an inverse azimuthal Fourier transform is applied to obtain complex and real-valued model projections in the observation space, referred to as $\mathcal{M}^{\pm}(t_j, \boldsymbol{x}, \theta'_k)$ and $\mathcal{P}^{\pm}(t_j, \boldsymbol{x}, \theta'_k)$ respectively. Here, owing to the known azimuthal symmetry of the model, $\{\theta'_k\}_{k=1..N'_\theta}$ can be arbitrary projection angles, particularly such that $N'_\theta > N_\theta = 6$, the actual number of holographic lines. This operation writes

$$\mathcal{P}^{\pm}(t_j, \boldsymbol{x}, \theta'_k) = \underbrace{\frac{1}{2N_\theta} \widehat{\mathcal{M}}^{\pm}(t_j, \boldsymbol{x})\, \mathrm{e}^{\mathrm{i}\theta'_k}}_{\mathcal{M}^{\pm}} + \quad \text{c.c.} \tag{4.12}$$

and equally-spaced model projections on a half-circle were obtained with $\theta'_k = k\pi/N'_\theta$. Similarly to tomographic reconstruction of the mean density field in section 4.1, $N'_\theta = 64$ was observed to provide well resolved density reconstructions.

4.2.6. *Density reconstruction of the helical structure*

The 3D tomographic reconstructions obtained for $\mathcal{P}^+$ and $\mathcal{P}^-$ with two arbitrary values of Ω are illustrated using 3D contour plots in figures 22(a,b) respectively. Two laterally-translated median longitudinal cross-sections extracted at $y = 0$ and $z = 0$ (gray scales) and an axially-translated transverse cross-section at $x/D = 3.85$ (at the edge of the reconstructed domain, colored scales) are also displayed in each figure to further illustrate the internal density distribution of these large-scale structures. An animation is provided as additional material for better 3D visualization.

As previously indicated, the projected reduced models $\mathcal{P}^{\pm}$ clearly describe a helical structure, particularly visible in the external shear layer between the two shock-cells, with two possible azimuthal directions of rotation. In the longitudinal cross-sectional planes, this dynamical model yields apparent convection and growth of density fluctuations as would be expected from an azimuthal instability wave. A particular feature of this result is that the density fluctuations associated with this reconstructed helical structure extend into the interior of the jet. Large density fluctuations can be observed in the embedded shear layer of the first and second shock-cells. As seen in the transverse cross-sections showing colored contour plots, these internal fluctuations are out-of-phase with the fluctuations observed in the external jet mixing layer. Similar observations have been reported by Edgington-Mitchell et al. (2014a) who performed planar PIV measurements in an under-expanded jet at a NPR of 4.2 characterized by helical dynamics associated with a screech mode C. These authors suggested that the helical instability observed in the external jet shear layer was driving large velocity fluctuations in the jet embedded shear layers. Based on qualitative observations, they furthermore hypothesized that the motion of the reflected shocks may play an important role in the development of these inner shear layer fluctuations.

4.2.7. *Analysis of the reconstructed density fluctuations*

To investigate this point further, a more quantitative description of the density fluctuations captured by the present reduced model is provided in figure 23. The complex-valued version of the model $\mathcal{M}^{\pm}$ is considered instead of its real part $\mathcal{P}^{\pm}$ since the former intrinsically contains information about the spatial correlations of the density fluctuations. The amplitudes of the fluctuations normalized by ρ_j in a longitudinal plane of the jet are first displayed in

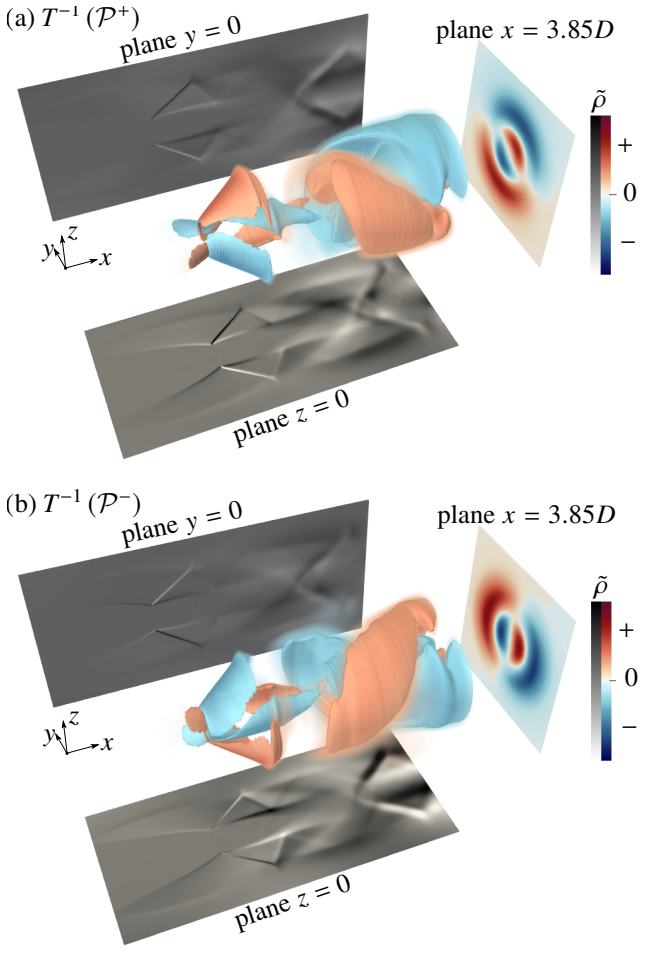


Figure 22: Illustrations of the 3D density fields obtained by tomographic reconstruction (noted T^{-1}) of the reduced dynamical models (a) $\mathcal{P}^+$ and (b) $\mathcal{P}^-$, for two arbitrary values of model phase Ω.

figure 23(a). These amplitudes are furthermore scaled by $2/\sqrt{2}$ to account for the contribution of the complex conjugate term in equation (4.12) to the overall density fluctuations and to provide root-mean-square estimates. With this scaling, this reduced model is shown to capture maximum rms density fluctuations of about $0.1\rho_j$ in the second shock-cell, an order of magnitude that is in agreement with values reported by Panda & Seasholtz (1999) using Rayleigh scattering measurements with phase-averaging on the screech noise. In this figure, the growth of the helical instability in the outer jet shear layer can be observed with a streamwise increase of the density fluctuations in the profiles located between the two shock-cells. Significant fluctuations are also found in the vicinity of the oblique reflected shock of the first shock-cell. As discussed by Panda (1998) and André et al. (2011), these fluctuations are the footprint of oblique shock oscillations that have been proposed to be induced either by upstream acoustic waves associated with the screech feedback loop or by instability waves growing in the outer mixing layer. The present quantitative results, and particularly the visualizations shown in figure 22, provide support for the presence of azimuthal shock oscillations for screech mode C, as suggested by Panda (1998). Similarly,

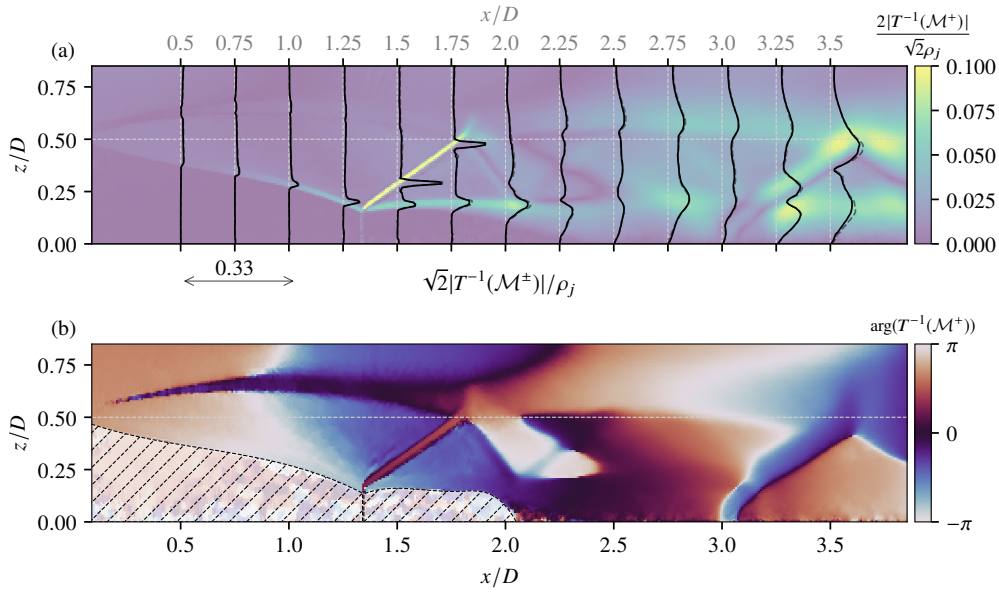


Figure 23: (a) Amplitude and (b) phase maps of the density fluctuations captured by tomographic reconstruction of the reduced complex model $\mathcal{M}^+$ in the longitudinal plane of the jet. In (a), the black solid lines (——) provide the profiles of fluctuation amplitude for $\mathcal{M}^+$ and the dark-gray dashed lines (- - -) give the profiles for $\mathcal{M}^-$. In (b), the core region of the jet over the first two nozzle diameters is hashed since the phase estimates in this region are extremely uncertain.

the density fluctuations observed around the reflected shock of the second shock-cell are also to be related to azimuthal shock oscillations, but with greater spatial dispersion due to larger cell motions.

Figure 23(a) further highlights the presence of intense density fluctuations in the embedded shear layers of both shock-cells. In the first, the fluctuations in the internal layer appear to grow moderately in the streamwise direction, up to the end of the shock-cell around $x = 2D$. This is in agreement with visualizations by Yip et al. (1989), obtained using Rayleigh scattering imaging, who observed that the reduced growth in the streamwise direction could be explained by the large convective Mach numbers in this region and a dampening of internal Kelvin–Helmholtz instabilities due to compressibility effects. From there, the internal mixing layer interacts with the expansion fan generated by the intersection of the first reflected shock with the outer mixing layer, yielding a significant radial diffusion of density fluctuations toward the jet axis. The embedded shear layer of the second shock-cell also displays intense but more diffuse density variations in the radial direction. Of particular interest, the amplitudes of density fluctuations appear to be very similar for $\mathcal{M}^+$ and $\mathcal{M}^-$, with only moderate differences in maximum amplitudes appearing downstream, for $x > 3.5D$, with $\mathcal{M}^-$ being slightly more intense. The different radii of the two circular orbits identified in the two POD modes phase space in figure 19 thus have a limited effect and do not significantly change the structure of the two isolated helical modes.

Valuable insights are finally given by the phase map shown in figure 23(b) that allows to identify phase links in the field of density fluctuations captured by $\mathcal{M}^{\pm}$. It is noted that the upstream core region of the jet is hashed since no reliable phase estimates could be obtained in this part of the flow where almost no density fluctuations were captured (see figure 23(a)). To begin with, the phase pattern of the standing wave previously identified in

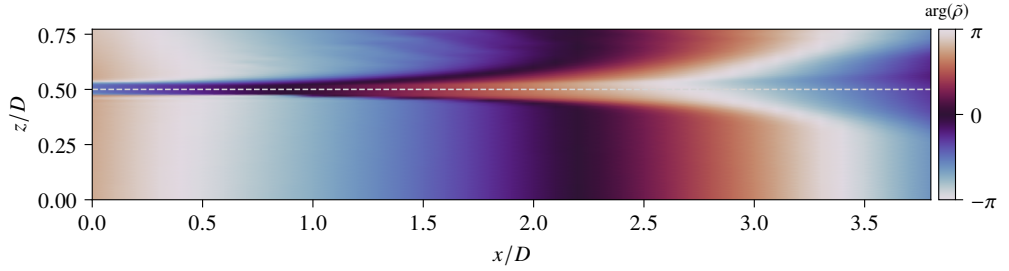


Figure 24: Phase map of density fluctuations evaluated using PSE in the longitudinal plane of a perfectly-expanded supersonic jet at $M_j = 1.7$, for a Strouhal number $\mathrm{St}_j = 0.23$ and an azimuthal wavenumber $m = 1$.

figure 13 in the external near-field of the jet can be clearly identified, with an axial wavelength of about $2.5D$. A smooth phase-coupling between this standing wave and the perturbations developing in the outer mixing layer is observed upstream and downstream of the first shock-cell, for $x > 1.0D$. Furthermore, the oblique shock oscillations in the two shock-cells are directly in phase with the density fluctuations captured in the region of interaction with the outer shear layer. This again indicates a strong coupling between shock oscillations and the helical Kelvin–Helmholtz (KH) instability wave developing in this outer mixing layer, in agreement with the main mechanism proposed in the literature (Panda 1998; André et al. 2011). The interior region of the jet, however, displays fluctuations that are generally out-of-phase with those found in the outer mixing layer and the oblique shock oscillations. First, the helical density fluctuations in the expansion fan of the first shock-cell are in approximate quadrature phase-shift relative to the shock oscillations. Second, considering any of the two shock-cells displayed, the density fluctuations associated with the oblique shock motions are in approximate anti-phase relative to the upstream and downstream density fluctuations. Of particular interest is a continuous large-scale variation of phase inside the jet, in the streamwise direction and across the shock waves. This large-scale internal phase distribution exhibits a phase jump across the outer shear layer but shows uniform variations in the embedded shear layers.

Based on these observations, it is proposed to interpret this out-of-phase link between fluctuations found in the embedded shear-layers and in the outer mixing layer (discarding the near-field standing wave pattern) as the consequence of a phase-shift between large-scale waves developing inside the jet and in the outer mixing layer. In these two regions of the jet, a similar approximate large-scale axial wavelength of about $3.5D$ is estimated. This value corresponds to about 2 shock-cell spacings and is identified as the footprint of the outer-layer KH instability wave having support in the entire jet (Edgington-Mitchell et al. 2021). This suggests that the phase differences observed between the two regions can be related to the classical phase jump across shear layers observed for KH instability waves, a feature commonly found in axial velocity fluctuations of KH modes (see Nogueira et al. (2021) for example), but which also appears in fields of density fluctuations. As an example, figure 24 displays the phase map of density fluctuations captured by Parabolized Stability Equations (PSE) (Herbert 1997; Sinha et al. 2014) applied to an analytic model of a perfectly-expanded supersonic jet (which is thus free of shock-cells and screech) at a similar Mach number $M_j = 1.71$, for an azimuthal wavenumber $m = 1$ and for a Strouhal number equivalent to that deduced from screech noise measurements obtained for the present under-expanded jet. The spatial distribution of phase values in the mixing layer and in the jet core is qualitatively in agreement with the large-scale variations identified in figure 23(b), displaying a similar

phase decrease radially toward the jet axis and providing support for the proposition. More significant differences in phase pattern in the outer jet region can be observed and are associated with the absence of the screech-related standing wave in this simple example, which serves only to highlight the internal structure of the KH instability wave. From this perspective, the helical density fluctuations found in the embedded shear layers in figure 23 are interpreted as being directly driven by the outer KH instability wave, suggesting that reflected shocks oscillations only play a minor or indirect role in the associated dynamics. It is emphasized, however, that this conclusion is based on spatio-temporal correlations rendered by a reduced model and that further experimental or numerical work should thus be considered to clarify its validity.

Finally, figure 23(b) suggests that a near-perfect phase match exists across the outer shear layer in the nozzle-lip region between the outer standing wave and the inner-jet large-scale fluctuations. While a phase-match condition between KH modes and upstream-traveling waves is to be expected in the receptivity region of the mixing layer for the resonant mechanism at work to be closed, it is interesting to observe that this appears to be accompanied by a phase match of density fluctuations in the two regions surrounding the initial shear layer.

5. Conclusion

The multi-view DHI setup detailed in this work has provided original insights into the structure of an under-expanded screeching supersonic jet in helical mode. More generally, this optical setup can be expected to be of interest for a broader class of aerothermal or compressible open-flows characterized by dynamical coherent structures presenting azimuthal symmetries. The main advantages of the presented technique are its fine optical phase measurement resolution (on the order of 100 µm for the present setup) providing sharp instantaneous images of shock waves and direct access to the azimuthal content of the flow projections using azimuthal Fourier transforms. However, some challenges should be highlighted. First, the optical layout can be relatively complex to implement and sensitive to vibrations. Second, the technique provides indirect access to the probed density fields since phase-unwrapping and tomographic reconstruction are necessary post-processing steps. Particularly, the limited number of interferometric lines used prevents any reliable density field reconstruction without taking advantage of azimuthal symmetries in the flow. Furthermore, the quality of the reconstructed density fields depends significantly on the tomographic reconstruction process. This study considered a regularized tomographic approach relying on Total Variation regularization to account for the presence of shock waves. While providing satisfactory results, improvements in the quality of the reconstructed density fields could be expected in future work by using higher-order regularization techniques such as Total Generalized Variation (TGV) regularization (Bredies et al. 2010), or newly developed learned regularization strategies (Gilton et al. 2020) increasing the level of a priori knowledge used in the reconstruction process. A final challenging topic that has yet to be addressed in depth and that is related to the choice of tomographic reconstruction approach concerns uncertainty quantification in the reconstructed density fields.

The use of POD applied to the main azimuthal Fourier mode of the flow projections revealed fine details about the main 3D dynamics of the jet. First, evidence of intermittency in the direction of rotation of the observed helical screech mode C is reported. This unexpected feature has not been observed previously to the authors' knowledge and is likely to depend on the jet facility (e.g., upstream flow conditions) or the nozzle geometry (e.g., lip thickness). This result is particularly interesting since the screech mode C is commonly thought to be stable and steady, as reported by Powell et al. (1992) for instance. The present results therefore suggest that a more thorough investigation of the receptivity mechanisms at work in

these jets should be conducted. It is important for such studies to emphasize that the present observation of switching in the direction of rotation using flow state projections can only be unambiguously obtained by using multiple observation lines. Relying on a single flow projection (as obtained with single-line BOS, schlieren imaging or DHI for example) would have obscured this result. In particular, applying POD to the snapshots obtained with a single DHI line yields only a single pair of real modes, in contrast to the results shown in figures 18 and 19 where two complex pairs have been identified.

Secondly, a forcing mechanism of the inner jet shear layer and reflected shocks by the main helical KH instability wave developing in the outer jet shear layer has been evidenced. This work complements the observations reported by Edgington-Mitchell et al. (2014a) and offers a physically-plausible explanation for the out-of-phase motions of the helical coherent structures observed in the two regions. Interestingly, Edgington-Mitchell et al. (2014a) additionally reported the presence of weak axisymmetric structures in the inner annular shear layer. Although not explicitly shown here, minor or suboptimal azimuthal POD modes (found for $m \neq 1$ in the azimuthal decomposition given in figure 15) have also been observed with the present measurements, but in both the outer and inner shear layers. In particular, weak axisymmetric modes in the inner shear layer have been found to be mainly accompanied by dominant outer-layer modes. Overall, the present study therefore suggests that the coherent dynamics of a screeching jet is driven primarily by the outer-layer instability waves, for both the preferred azimuthal mode and for the suboptimal modes. Investigations at various NPRs and for different screech modes should be considered to validate and explore the universality of this conclusion which could help to better understand the internal dynamics of these jets.

Funding. This study was performed within the framework of the internal research project MEROVEE3D at ONERA. It also received support from the French National Agency for Research (ANR) (grant agreement ANR-14-ASTR-0005-01).

Declaration of interests. The authors report no conflict of interest.

Author ORCID. O. Léon, https://orcid.org/0000-0002-2865-8037

Appendix A. Intertwining Radon and azimuthal Fourier transforms

The following theorem supporting the discussion of section 4.2.3 may already exist in the literature, but it has not been found by the authors. For the necessary prior definitions of the Radon transform and its natural domain, the reader is referred to Epstein (2008) for example. Here, $\mathcal{R}f(r,\theta)$ refers to the Radon transform of f on a line L whose distance to the origin is $|r|$ with $r \in \mathbb{R}$ and whose angle in the plane is $\theta \in [0, 2\pi[$.

Theorem 1. *Let f be an absolutely integrable function of the plane in the natural domain of $\mathcal{R}$. Let f be defined in polar coordinates on $\mathbb{R} \times [0, 2\pi[$ with a decomposition in Fourier series that writes*

$$f(\rho,\varphi) = \sum_{m\in\mathbb{Z}} \tilde{f}_m(\rho,\varphi) \tag{A 1}$$

with $\tilde{f}_m(\rho,\varphi) = \widehat{f}_m(\rho)\mathrm{e}^{\mathrm{i}m\varphi}$. Then,

$$\mathcal{R}\tilde{f}_m(r,0) = \frac{1}{2\pi}\int_0^{2\pi} \mathcal{R}f(r,\theta)\mathrm{e}^{-\mathrm{i}m\theta}\mathrm{d}\theta\,. \tag{A 2}$$

In other words, the Radon transform applied to an azimuthal Fourier mode of an object defined in physical space corresponds to the azimuthal Fourier mode of Radon projections

of the object in the observation space. The Radon transform thus preserves azimuthal symmetries and can then be viewed as an equivariant map under azimuthal Fourier transforms.

Proof. Using the Fourier series of f and the linearity of the Radon transform,

$$\mathcal{R}f(r,\theta) = \sum_{m'\in\mathbb{Z}} \mathcal{R}\tilde{f}_{m'}(r,\theta)\,. \tag{A 3}$$

Using proposition 6.1.4 from Epstein (2008) that considers the effect of rigid rotations on the Radon transform of a function in the plane, one can write

$$\mathcal{R}\tilde{f}_{m'}(r,\theta) = \mathcal{R}\tilde{f}_{m',\theta}(r,0) \tag{A 4}$$

with $\tilde{f}_{m',\theta}$ denoting rotation of $\tilde{f}_{m'}(\rho,\varphi)$ by an angle θ, thus such that

$$\tilde{f}_{m',\theta}(\rho,\varphi) = \widehat{f}_{m'}(\rho)\mathrm{e}^{\mathrm{i}m'(\varphi+\theta)} = \tilde{f}_{m'}(\rho,\varphi)\mathrm{e}^{\mathrm{i}m'\theta}\,. \tag{A 5}$$

Consequently,

$$\mathcal{R}f(r,\theta)\mathrm{e}^{-\mathrm{i}m\theta} = \sum_{m'\in\mathbb{Z}} \left(\mathcal{R}\tilde{f}_{m'}(r,0)\mathrm{e}^{\mathrm{i}(m'-m)\theta}\right) \tag{A 6}$$

and finally

$$\frac{1}{2\pi}\int_0^{2\pi} \mathcal{R}f(r,\theta)\mathrm{e}^{-\mathrm{i}m\theta}\mathrm{d}\theta = \sum_{m'\in\mathbb{Z}} \frac{\mathcal{R}\tilde{f}_{m'}(r,0)}{2\pi}\int_0^{2\pi} \mathrm{e}^{\mathrm{i}(m'-m)\theta}\mathrm{d}\theta = \mathcal{R}\tilde{f}_m(r,0)\,, \tag{A 7}$$

where in the last step the orthogonality of the Fourier basis yields only one non-zero term for $m = m'$.

REFERENCES

van Aarle, Wim, Palenstijn, Willem Jan, Beenhouwer, Jan De, Altantzis, Thomas, Bals, Sara, Batenburg, K. Joost & Sijbers, Jan 2015 The ASTRA toolbox: A platform for advanced algorithm development in electron tomography. *Ultramicroscopy* **157**, 35–47.

Addy, A. L. 1981 Effects of axisymmetric sonic nozzle geometry on Mach disk characteristics. *AIAA Journal* **19** (1), 121–122.

André, Benoît, Castelain, Thomas & Bailly, Christophe 2011 Shock-tracking procedure for studying screech-induced oscillations. *AIAA Journal* **49** (7), 1563–1566.

Atcheson, Bradley, Ihrke, Ivo, Heidrich, Wolfgang, Tevs, Art, Bradley, Derek, Magnor, Marcus & Seidel, Hans-Peter 2008 Time-resolved 3D capture of non-stationary gas flows. *ACM Trans. Graph.* **27** (5), 132:1–132:9.

Beck, Amir & Teboulle, Marc 2009 A fast iterative shrinkage-thresholding algorithm for linear inverse problems. *SIAM Journal on Imaging Sciences* **2** (1), 183–202.

Bredies, Kristian, Kunisch, Karl & Pock, Thomas 2010 Total generalized variation. *SIAM Journal on Imaging Sciences* **3** (3), 492–526.

Chambolle, Antonin & Pock, Thomas 2010 A first-order primal-dual algorithm for convex problems with applications to imaging. *Journal of Mathematical Imaging and Vision* **40** (1), 120–145.

Chambolle, Antonin & Pock, Thomas 2016 An introduction to continuous optimization for imaging. *Acta Numerica* **25**, 161–319.

Champagnat, Frédéric, Nicolas, F., Olchewsky, F., Donjat, D., Essaïdi, Z. & Desse, J.-M. 2018 Comparison of BOS and digital holography on an underexpanded jet. In Proceedings 18th International Symposium on Flow Visualization. ETH Zurich.

Davies, MG & Oldfield, DES 1962 Tones from a choked axisymmetric jet. I. cell structure, eddy velocity and source locations. *Acta Acustica united with Acustica* **12** (4), 257–267.

Desse, J.-M. & Olchewsky, F. 2016 Digital holographic interferometry for analysing high density gradients in Fluid Mechanics. In Tech Book, edited by Dr. Martina Usljebrka.

Dillmann, A., Wetzel, T. & Soeller, C. 1998 Interferometric measurement and tomography of the density field of supersonic jets. *Experiments in Fluids* **25** (5-6), 375–387.

Doleček, Roman, Psota, Pavel, Lédl, Vít & Vít, Tomáš 2016 Heat and mass transfer measurement using method of digital holographic tomography. In Optics and Measurement International Conference 2016, , vol. 10151, p. 1015119. International Society for Optics and Photonics.

Doleček, R., Psota, P., Lédl, V., Vít, T., Václavík, J. & Kopecký, V. 2013 General temperature field measurement by digital holography. *Appl. Opt.* **52** (1), A319–A325.

Edgington-Mitchell, Daniel 2019 Aeroacoustic resonance and self-excitation in screeching and impinging supersonic jets – a review. *International Journal of Aeroacoustics* **18** (2-3), 118–188.

Edgington-Mitchell, Daniel, Honnery, Damon R. & Soria, Julio 2014a The underexpanded jet Mach disk and its associated shear layer. *Physics of Fluids* **26** (9), 096101.

Edgington-Mitchell, Daniel, Jaunet, Vincent, Jordan, Peter, Towne, Aaron, Soria, Julio & Honnery, Damon 2018 Upstream-travelling acoustic jet modes as a closure mechanism for screech. *Journal of Fluid Mechanics* **855**.

Edgington-Mitchell, Daniel, Oberleithner, Kilian, Honnery, Damon R. & Soria, Julio 2014b Coherent structure and sound production in the helical mode of a screeching axisymmetric jet. *Journal of Fluid Mechanics* **748**, 822–847.

Edgington-Mitchell, Daniel, Wang, Tianye, Nogueira, Petronio, Schmidt, Oliver, Jaunet, Vincent, Duke, Daniel, Jordan, Peter & Towne, Aaron 2021 Waves in screeching jets. *Journal of Fluid Mechanics* **913**.

Epstein, C.L. 2008 Introduction to the Mathematics of Medical Imaging. Other Titles in Applied Mathematics 9780898716429. SIAM Society for Industrial and Applied Mathematics.

Franquet, Erwin, Perrier, Vincent, Gibout, Stéphane & Bruel, Pascal 2015 Free underexpanded jets in a quiescent medium: A review. *Progress in Aerospace Sciences* **77**, 25–53.

Ghiglia, Dennis C & Pritt, Mark D 1998 Two-dimensional phase unwrapping: theory, algorithms, and software, , vol. 4. Wiley New York.

Gilton, Davis, Ongie, Greg & Willett, Rebecca 2020 Neumann networks for linear inverse problems in imaging. *IEEE Transactions on Computational Imaging* **6**, 328–343.

Gojon, Romain, Bogey, Christophe & Mihaescu, Mihai 2018 Oscillation modes in screeching jets. *AIAA Journal* **56** (7), 2918–2924.

Grauer, Samuel J., Unterberger, Andreas, Rittler, Andreas, Daun, Kyle J., Kempf, Andreas M. & Mohri, Khadijeh 2018 Instantaneous 3D flame imaging by background-oriented schlieren tomography. *Combustion and Flame* **196**, 284–299.

Hansen, Per Christian 1998 Rank-deficient and discrete ill-posed problems: numerical aspects of linear inversion. SIAM.

Hansen, Per Christian 1999 The L-curve and its use in the numerical treatment of inverse problems .

Herbert, Thorwald 1997 Parabolized Stability Equations. *Annual Review of Fluid Mechanics* **29** (1), 245–283.

Herraez, M.A., Burton, D.R., Lalor, M.J. & Gdeisat, M.A. 2002 Fast two-dimensional phase unwrapping algorithm based on sorting by reliability following a noncontinuous path. *Applied Optics* **41** (35), 7437–7444.

Holmes, Philip, Lumley, John L, Berkooz, Gahl & Rowley, Clarence W 2012 Turbulence, coherent structures, dynamical systems and symmetry. Cambridge university press.

Idier, Jérôme 2010 Bayesian approach to Inverse problems, , vol. 35. John Wiley & Sons.

Ishino, Yojiro, Hayashi, Naoki, Razak, Ili Fatimah Bt Abd, Kato, Takahiro, Kurimoto, Yudai & Saiki, Yu 2015 3d-CT(computer tomography) measurement of an instantaneous density distribution of turbulent flames with a multi-directional quantitative schlieren camera (reconstructions of high-speed premixed burner flames with different flow velocities). *Flow, Turbulence and Combustion* **96** (3), 819–835.

Kazantsev, D. 2019 TOmographic MOdel-BAsed Reconstruction software. Software available at https://github.com/dkazanc/ToMoBAR.

Lanen, T. A. W. M., Bakker, P. G. & Bryanston-Cross, P. J. 1992 Digital holographic interferometry in high-speed flow research. *Experiments in Fluids* **13** (1), 56–62.

Lang, Henning M., Oberleithner, Kilian, Paschereit, C. Oliver & Sieber, Moritz 2017 Measurement of the fluctuating temperature field in a heated swirling jet with BOS tomography. *Experiments in Fluids* **58** (7).

Lanzillotta, L., Léon, O., Donjat, D. & Le Besnerais, G. 2019 3D density reconstruction of a screeching supersonic jet by synchronized multi-camera background oriented schlieren. In Proceedings of 8th EUCASS, Madrid.

Matulka, Robert D. & Collins, Daniel J. 1971 Determination of three-dimensional density fields from holographic interferograms. *Journal of Applied Physics* **42** (3), 1109–1119.

Nicolas, F., Donjat, D., Léon, O., Besnerais, G. Le, Champagnat, F. & Micheli, F. 2017 3D reconstruction of a compressible flow by synchronized multi-camera BOS. *Experiments in Fluids* **58** (5).

Nicolas, F., Todoroff, V., Plyer, A., Le Besnerais, G., Donjat, D., Micheli, F., Champagnat, F., Cornic, P. & Le Sant, Y. 2016 A direct approach for instantaneous 3D density field reconstruction from background-oriented schlieren (BOS) measurements. *Experiments in Fluids* **57** (1), 1–21.

Nogueira, Petrônio A.S., Jaunet, Vincent, Mancinelli, Matteo, Jordan, Peter & Edgington-Mitchell, Daniel 2022 Closure mechanism of the a1 and a2 modes in jet screech. *Journal of Fluid Mechanics* **936**.

Nogueira, Petrônio A.S., Jordan, Peter, Jaunet, Vincent, Cavalieri, André V.G., Towne, Aaron & Edgington-Mitchell, Daniel 2021 Absolute instability in shock-containing jets. *Journal of Fluid Mechanics* **930**.

Oberleithner, K., Sieber, M., Nayeri, C. N., Paschereit, C. O., Petz, C., Hege, H.-C., Noack, B. R. & Wygnanski, I. 2011 Three-dimensional coherent structures in a swirling jet undergoing vortex breakdown: stability analysis and empirical mode construction. *Journal of Fluid Mechanics* **679**, 383–414.

Olchewsky, F., Essaidi, Z., Desse, J.M. & Champagnat, F. 2018 3d reconstrcutions of jets by multidirectional digital holographic tomography. In ISFV 2018. Zurich.

Paleo, Pierre 2017 Iterative Methods in regularized tomographic reconstruction. Theses, Université Grenoble Alpes.

Panda, J. 1998 Shock oscillation in underexpanded screeching jets. *Journal of Fluid Mechanics* **363**, 173–198.

Panda, J. & Seasholtz, R. G. 1999 Measurement of shock structure and shock–vortex interaction in underexpanded jets using rayleigh scattering. *Physics of Fluids* **11** (12), 3761–3777.

Picart, Pascal, Gross, Michel & Marquet, Pierre 2015 Basic Fundamentals of Digital Holography, chap. 1, pp. 1–66. John Wiley and Sons, Ltd.

Powell, A 1953 On the mechanism of choked jet noise. *Proceedings of the Physical Society. Section B* **66** (12), 1039–1056.

Powell, Alan 2010 On Prandtl's formulas for supersonic jet cell length. *International Journal of Aeroacoustics* **9** (1-2), 207–236.

Powell, Alan, Umeda, Yoshikuni & Ishii, Ryuji 1992 Observations of the oscillation modes of choked circular jets. *The Journal of the Acoustical Society of America* **92** (5), 2823–2836.

Raman, G. 1999 Supersonic jet screech: half-century from powell to the present. *Journal of Sound and Vibration* **225** (3), 543 – 571.

Rodrigues, Neil, Brown, Alex, Meyer, Terrence & Lucht, Robert 2021 0.1-5 MHz ultrahigh-speed gas densitydistributions using digital holographicinterferometry. *Applied Optics* .

Schmid, Peter J., Violato, Daniele & Scarano, Fulvio 2012 Decomposition of time-resolved tomographic PIV. *Experiments in Fluids* **52** (6), 1567–1579.

Schnars, Ulf, Falldorf, Claas, Watson, John & Jüptner, Werner 2014 Digital holography. In Digital Holography and Wavefront Sensing, pp. 39–68. Springer Berlin Heidelberg.

Sinha, Aniruddha, Rodríguez, Daniel, Brès, Guillaume A. & Colonius, Tim 2014 Wavepacket models for supersonic jet noise. *Journal of Fluid Mechanics* **742**, 71–95.

Sipkens, T A, Grauer, S J, Steinberg, A M, Rogak, S N & Kirchen, P 2021 New transform to project axisymmetric deflection fields along arbitrary rays. *Measurement Science and Technology* **33** (3), 035201.

Sirovich, Lawrence 1987 Turbulence and the dynamics of coherent structures. i. coherent structures. *Quarterly of applied mathematics* **45** (3), 561–571.

Smits, A.J. 2012 Flow Visualization: Techniques and Examples. Imperial College Press.

Snyder, Ray & Hesselink, Lambertus 1988 Measurement of mixing fluid flows with optical tomography. *Optics Letters* **13** (2), 87.

Söller, C., Wenskus, R., Middendorf, P., Meier, G. E. A. & Obermeier, F. 1994 Interferometric tomography for flow visualization of density fields in supersonic jets and convective flow. *Applied Optics* **33** (14), 2921.

Sugawara, S., Nakao, S., Miyazato, Y., Ishino, Y. & Miki, K. 2020 Three-dimensional reconstruction of a microjet with a Mach disk by Mach-Zehnder interferometers. *Journal of Fluid Mechanics* **893**.

Sweeney, D.W. & Vest, C.M. 1974 Measurement of three-dimensional temperature fields above heated surfaces by holographic interferometry. *International Journal of Heat and Mass Transfer* **17** (12), 1443–1454.

Takeda, Mitsuo, Ina, Hideki & Kobayashi, Seiji 1982 Fourier-transform method of fringe-pattern analysis for computer-based topography and interferometry. *J. Opt. Soc. Am.* **72** (1), 156–160.

Tikhonov, A. & Arsenin, V. 1977 Solutions of ill-posed problems. Winston.

Timmerman, B.H., Watt, D.W. & Bryanston-Cross, P.J. 1999 Quantitative visualization of high-speed 3D turbulent flow structures using holographic interferometric tomography. *Optics & Laser Technology* **31** (1), 53–65.

Timmerman, B & Watt, D W 1995 Tomographic high-speed digital holographic interferometry. *Measurement Science and Technology* **6** (9), 1270–1277.

Watt, D. W. & Vest, C. M. 1987 Digital interferometry for flow visualization. *Experiments in Fluids* **5** (6), 401–406.

Watt, D. W. & Vest, C. M. 1990 Turbulent flow visualization by interferometric integral imaging and computed tomography. *Experiments in Fluids* **8** (6), 301–311.

Xiong, Yuan, Kaufmann, Tim & Noiray, Nicolas 2020 Towards robust BOS measurements for axisymmetric flows. *Experiments in Fluids* **61** (8).

Yip, B., Lyons, K., Long, M., Mungal, M. G., Barlow, R. & Dibble, R. 1989 Visualization of a supersonic underexpanded jet by planar rayleigh scattering. *Physics of Fluids A: Fluid Dynamics* **1** (9), 1449–1449.